



THE UNIVERSITY *of* EDINBURGH

Edinburgh Research Explorer

AN EXPERIMENTAL STUDY OF TRACE ELEMENT FLUXES FROM SUBDUCTED OCEANIC CRUST

Citation for published version:

Carter, LB, Skora, S, Blundy, J, De Hoog, C-J & Elliott, T 2015, 'AN EXPERIMENTAL STUDY OF TRACE ELEMENT FLUXES FROM SUBDUCTED OCEANIC CRUST', *Journal of Petrology*, vol. 56, no. 8, pp. 1585-1606. <https://doi.org/10.1093/petrology/egv046>

Digital Object Identifier (DOI):

[10.1093/petrology/egv046](https://doi.org/10.1093/petrology/egv046)

Link:

[Link to publication record in Edinburgh Research Explorer](#)

Document Version:

Early version, also known as pre-print

Published In:

Journal of Petrology

General rights

Copyright for the publications made accessible via the Edinburgh Research Explorer is retained by the author(s) and / or other copyright owners and it is a condition of accessing these publications that users recognise and abide by the legal requirements associated with these rights.

Take down policy

The University of Edinburgh has made every reasonable effort to ensure that Edinburgh Research Explorer content complies with UK legislation. If you believe that the public display of this file breaches copyright please contact openaccess@ed.ac.uk providing details, and we will remove access to the work immediately and investigate your claim.





Draft Manuscript for Review

AN EXPERIMENTAL STUDY OF TRACE ELEMENT FLUXES FROM SUBDUCTED OCEANIC CRUST

Journal:	<i>Journal of Petrology</i>
Manuscript ID:	JPET-Jul-14-0099.R2
Manuscript Type:	Original Manuscript
Date Submitted by the Author:	08-Jul-2015
Complete List of Authors:	Carter, Laura; University Of Bristol, Skora, Susanne; University of Bristol, Earth Sciences Blundy, Jon; University Of Bristol, De Hoog, Jan; University of Edinburgh, School of Geosciences Elliott, Tim; University Of Bristol,
Keyword:	MORB, trace element, experimental petrology, island arc, partial melting, subduction

SCHOLARONE™
Manuscripts

AN EXPERIMENTAL STUDY OF TRACE ELEMENT FLUXES FROM
SUBDUCTED OCEANIC CRUST

Carter, L.B.^{1,2}, Skora, S.^{1,3*}, Blundy, J.¹, De Hoog, J.C.M⁴, Elliott, T.¹

¹School of Earth Sciences, University of Bristol, Wills Memorial Building, Queen’s Road,
Bristol BS8 1RJ, UK

²Department of Earth Sciences, Rice University, 6100 Main Street, Houston, Texas 77005,
USA

³Department Erdwissenschaften, ETH Zürich, Clausiusstrasse 25NW, 8092 Zürich,
Switzerland

⁴School of GeoSciences, University of Edinburgh, Grant Institute, The King’s Buildings,
James Hutton Road, Edinburgh EH9 3FE, UKF

*corresponding author: Susanne.Skora@erdw.ethz.ch

Key words: Arc volcanics; experimental petrology; MORB; partial melting; subduction.

ABSTRACT

We have determined experimentally the hydrous phase relations and trace element partitioning behaviour of ocean floor basalt protoliths at pressures and temperatures (3 GPa, 750-1000°C) relevant to melting in subduction zones. To avoid potential complexities associated with trace element doping of starting materials we have used natural, pristine mid-ocean ridge basalt (MORB from Kolbeinsey Ridge) and altered oceanic crust (AOC from DSDP leg 46, ~20°N Atlantic). Approximately 15 wt % water was added to starting materials to simulate fluid fluxing from dehydrating serpentinite underlying the oceanic crust. The vapour-saturated solidus is sensitive to basalt K₂O content, decreasing from 825±25°C in MORB (~0.04 wt % K₂O) to ~750°C in AOC (~0.25 wt % K₂O). Textural evidence indicates that near-solidus fluids are sub-critical in nature. The residual solid assemblage in both MORB and AOC experiments is dominated by garnet and clinopyroxene, with accessory kyanite, epidote, Fe-Ti oxide and rutile (plus quartz/coesite and apatite below the solidus). Trace element analyses of quenched silica-rich melts show a strong temperature dependence of key trace elements. In contrast to the trace element-doped starting materials of previous studies, we do not observe residual allanite. Instead abundant residual epidote provides the host for thorium and light rare earth elements (LREE), preventing LREE from being released (Σ LREE<3 ppm at 750-900°C). Elevated Ba/Th ratios, characteristic of many arc basalts, are found to be generated within a narrow temperature field above the breakdown temperature of phengite, but below exhaustion of epidote. Melts with Ba/Th >1500 and La/Sm_{PUM} (PUM=primitive upper mantle) ~1, most closely matching the geochemical signal of arc lavas worldwide, were generated from AOC at 800-850°C.

1
2
3
4
5
6
7
8
9
10
11
12
13
14
15
16
17
18
19
20
21
22
23
24
25
26
27
28
29
30
31
32
33
34
35
36
37
38
39
40
41
42
43
44
45
46
47
48
49
50
51
52
53
54
55
56
57
58
59
60

47 **INTRODUCTION**

48 Volcanic arc basalts are widely considered to form from a mantle wedge source region
49 comprising a ternary mixture of hydrous melt from subducted sediment, hydrous fluid (or
50 melt) from (altered) mafic oceanic crust and depleted mantle peridotite (e.g. Elliott, 2003).
51 The distinct trace element chemistry of basalts from different arcs can be ascribed to
52 differing proportions of these three components, reflecting a variation both in inputs to the
53 subduction system and in its thermal structure. Consequently the phase relations of the
54 different subducted components are important to determining under what conditions fluids
55 and melts are generated beneath arcs. If the pressure-temperature dependence of the stability
56 of key residual phases in subducted lithologies can be quantified then potentially the trace
57 element chemistry of arc basalts can be used to infer slab-top temperatures beneath volcanic
58 arcs (e.g. Cooper *et al.*, 2012; Hermann & Spandler, 2008; Klimm *et al.*, 2008; Plank *et al.*,
59 2009). The primary objective of this study is to explore the trace element chemistry of
60 hydrous partial melts associated with ocean floor basalts under subduction zone conditions.

61 Subducted slabs contain H₂O in the form of hydrous minerals, such as amphibole,
62 epidote, micas and serpentine. The breakdown of these minerals during subduction zone
63 metamorphism leads to progressive dehydration of the slab, releasing hydrous fluids into the
64 overlying mantle wedge (e.g. Schmidt & Poli, 1998). If slab temperatures are high enough,
65 as suggested by recent models (e.g. Syracuse *et al.*, 2010; van Keken *et al.*, 2002),
66 dehydration melting of the slab will occur, giving rise to hydrous, silica-rich melts that may
67 similarly ascend into the wedge. Thus both fluid and melt may be extracted from the slab
68 depending on the subduction zone geotherm. If each slab lithology behaves as a closed
69 system during subduction zone metamorphism, the only H₂O available in subducted basalt is

1
2
3
4
5
6
7
8
9
10
11
12
13
14
15
16
17
18
19
20
21
22
23
24
25
26
27
28
29
30
31
32
33
34
35
36
37
38
39
40
41
42
43
44
45
46
47
48
49
50
51
52
53
54
55
56
57
58
59
60

70 that structurally bound in hydrous minerals in the basalt itself. Dehydration melting of such
71 basalt occurs at relatively high temperatures that may only be achieved where the subducted
72 crust is young and therefore hot. Consequently, there is a long-standing debate as to whether
73 sub-solidus fluids or supra-solidus hydrous melts are the primary agent of slab-wedge
74 chemical transfer in subduction zones. Such a simple dichotomy is complicated by the fact
75 that at sufficiently high pressures silicate melts and hydrous fluids are completely miscible
76 (above the so-called second critical endpoint) rendering moot any distinction between fluid
77 and melt. Moreover, the dehydration of serpentine in ultramafic portions of the slab (Ulmer
78 & Trommsdorff, 1995) may flux overlying basaltic and sedimentary portions with H₂O, such
79 that dehydration melting of subducted basalt may not be the only melt-producing
80 mechanism. More in-depth summaries of subduction zone processes can be found in the
81 recent reviews of Spandler & Pirard (2013) and Schmidt & Poli (2014). Our experiments
82 were designed explicitly to test this flux-melting mechanism by using starting materials to
83 which H₂O contents exceeded those that could be contained within hydrous minerals alone.
84 In that sense our experiments build upon those of Kessel *et al.* (2005a, 2005b), Klimm *et al.*
85 (2008), Prouteau *et al.* (1999, 2001), and Ryabchikov *et al.* (1996).

86 In order to replicate experimentally the phase relations of hydrous ocean floor basalts
87 it is important to take account of the chemical effects of alteration that occur on the sea floor.
88 Subducted basalts range in composition from pristine mid-ocean ridge basalts (hereafter
89 “MORB”), unmodified since eruption, to hydrothermally modified, altered oceanic crust
90 (hereafter “AOC”) that characterises the upper pillow lavas and sheeted dykes (e.g. Alt *et al.*,
91 1989). The nature of sea-floor alteration depends on the temperature of hydrothermal
92 interaction (e.g. Humphris & Thompson, 1978; Mottl, 1983; Thompson, 1983) and, although

1
2
3
4
5
6
7
8
9
10
11
12
13
14
15
16
17
18
19
20
21
22
23
24
25
26
27
28
29
30
31
32
33
34
35
36
37
38
39
40
41
42
43
44
45
46
47
48
49
50
51
52
53
54
55
56
57
58
59
60

93 its chemical signature is spatially variable, both laterally and vertically (e.g. Kelley *et al.*,
94 2003), the key chemical changes relative to MORB are an overall rise in alkalis and the
95 volatile components sulphur, water and carbon dioxide, and to a lesser extent uranium (e.g.
96 Bach *et al.*, 2003; Gillis & Robinson, 1988; Kelley *et al.*, 2003; Melson, 1968; Mottl, 1983;
97 Seyfried *et al.*, 1988; Staudigel & Plank, 1996; Staudigel *et al.*, 1981a, 1981b). Previous
98 experimental studies have attempted to capture this chemical variability by using either
99 synthetic MORB (e.g. K-free MORB: Kessel *et al.*, 2005a, 2005b; KCMASH: Hermann &
100 Green, 2001; anhydrous MORB: Yasuda *et al.*, 1994; altered MORB: Klimm *et al.*, 2008;
101 Ryabchikov *et al.*, 1996) or metamorphosed material (e.g. amphibolite: Kogiso *et al.*, 1997;
102 Rapp & Watson, 1995; synthetic eclogite: Klemme *et al.*, 2002; Pertermann & Hirschmann,
103 2003). In several cases the starting materials were doped with trace elements to facilitate
104 trace element analysis of experimental run products and enhance the stability of accessory
105 phases (e.g. Klimm *et al.*, 2008). The first aim of our study was to remove the uncertainties
106 inherent in the use of synthetic and/or trace element-doped starting samples by using natural
107 ocean floor basalts. The second aim was to explore changes in phase petrology and trace
108 element partitioning that arises from chemical differences between MORB and AOC.

109
110 **METHODS**

111 **Starting Materials**

112 Sample materials used for this study were splits of rock powder that were used for other
113 geochemical studies. The first sample (“MORB”) is a pristine MORB tholeiite (37DS-1)
114 from the Kolbeinsey Ridge, retrieved from 67.08°N, 18.75°W between the Tjörnes and Spar
115 Fracture Zones, at a depth of 170 m (Devey *et al.*, 1994). This sample is extremely fresh and

unaltered, though slightly lower in TiO_2 and more depleted compared to average MORB given in Hofmann (1988, Table 1). Dredged basalts from this site are described as being mostly glassy with less than 10% (modal) phenocrysts (olivine and minor plagioclase and spinel for 37DS-1). The $f\text{O}_2$ of MORB is generally around the QFM buffer, amounting to an average $\text{Fe}^{3+}/\text{Fe}^{\text{tot}} \approx 0.16$ (e.g. Cottrell & Kelley, 2011).

The second sample (“AOC”) is an altered basalt (15-3, A3, 83-94 cm) from DSDP leg 46 Hole 396B near the Mid-Atlantic Ridge at a latitude of 23°N and a depth of ~ 240 m. This particular horizon is not described in the ODP report, but comes from a massive lava stream of subunit A3. Other samples from this subunit are described as porphyritic basalts (approx. 15-25% phenocrysts in leg 46 basalts), containing olivine and plagioclase phenocrysts with Ca-rich clinopyroxene in the groundmass and spinel. The massive lava is similar to overlying pillow basalts which can show secondary palagonite, Fe-Mn oxide, smectite, mica, zeolite and carbonate (e.g. Dungan *et al.*, 1979; Sato *et al.*, 1979). The seafloor-metasomatised parts of the lava unit exhibit elevated concentrations of H_2O (≈ 2 wt %), K_2O (≈ 0.3 wt %), Fe_2O_3 ($\text{Fe}^{3+}/\text{Fe}^{\text{tot}} \approx 0.3-0.5$; $f\text{O}_2 > \text{QFM}$), as well as some other elements (e.g. S, Rb) (e.g. Dungan *et al.*, 1979). Although carbon is also commonly enriched in basalts during sea floor alteration, we do not find evidence for significant amounts of CO_2 in our selected samples (a carbonate phase would be expected at least in the sub-solidus experiment, e.g. Molina & Poli, 2000).

In Table 1, we compare the major and trace element composition of our starting materials to average MORB (Hofmann, 1988) and AOC (Kelley *et al.*, 2003), as well as to some other experimental starting materials to which we later compare our results. A significant contrast between both starting material compositions is the low K_2O content of

1
2
3
4
5
6
7
8
9
10
11
12
13
14
15
16
17
18
19
20
21
22
23
24
25
26
27
28
29
30
31
32
33
34
35
36
37
38
39
40
41
42
43
44
45
46
47
48
49
50
51
52
53
54
55
56
57
58
59
60

MORB (roughly comparable to Kessel *et al.* 2005b) versus the order of magnitude higher K₂O content of AOC (roughly comparable to that reported by Green & Adam, 2003 and Klimm *et al.*, 2008). Other differences are marked by elevated Na₂O and TiO₂, as well as reduced MgO contents in the AOC sample.

Experimental Techniques

Both starting materials were repeatedly ground with a mortar and pestle and then dried to produce a homogeneous powder. Distilled water (approx. 1.8 µl) was injected into acid-cleaned and annealed Au (T<1000°C) or Au₈₀Pd₂₀ (T≥1000°C) capsules using a Hamilton microsyringe (5 µl). Inaccuracies in injecting small quantities of water are compensated by adjusting the amount of rock powder that is added afterwards such that final H₂O contents were around 15 wt %. The capsules were welded shut using a PUK microwelder. The negligible heating of the welder ensures that H₂O is retained in the capsules, as verified by weighing the water-bearing capsules before and after welding. The experimental cell consisted of inner spacers of crushable alumina, a graphite furnace, outer sleeve of salt and Pyrex, and a W₉₅/Re₅-W₇₅/Re₂₅ (Type “D”), alumina-sheathed axial thermocouple. The friction coefficient for this assembly is 3% (McDade *et al.*, 2002). No account was taken of any pressure effect on thermocouple e.m.f.. Experiments were run in ½-inch, end-loaded piston-cylinder apparatus at the University of Bristol using the ‘hot-piston-in’ method. Experiments were conducted at a pressure (P) of 3 GPa; experimental temperatures (T) ranged between 750-1000°C. The pressure was selected to lie close to the average depth of the Wadati-Benioff zone worldwide (≈105 km, Syracuse & Abers, 2006). Temperatures were selected to bracket the solidus and are in rough agreement with recent thermal models

of slab-top temperatures beneath arcs (e.g. Cooper *et al.*, 2012; Syracuse *et al.*, 2010; van Keken *et al.*, 2002). Run durations were 2 to 7 days, in inverse proportion to temperature. Supra-liquidus runs were carried out at 1.5 GPa and $\geq 1325^\circ\text{C}$ to glass both starting materials for analysis. Runs were quenched by turning off the power.

One experiment was repeated at ETH Zürich after the original showed signs of disequilibrium (AOC 750°C run, lack of garnet). The same method and furnace assembly were used, but with a different thermocouple to Bristol (Pt₉₄/Rh₆-Pt₇₀/Rh₃₀; Type “B”). Most importantly, this run was seeded with 2 wt % of gem quality garnet (composition $\approx \text{Py}_{56}\text{Alm}_{37}\text{Gross}_1\text{Spess}_1\text{Andr}_5$; $< 7\ \mu\text{m}$ fraction).

No attempt was made to control or monitor $f\text{O}_2$. Different pressure-cell assemblies can lead to variable $f\text{O}_2$ conditions in experiments (e.g., Truckenbrodt *et al.*, 1997), despite the use of a graphite furnace. For our assembly, in-house estimates of the $f\text{O}_2$ in Bristol lie in the range $\text{NNO}+2(\pm 1)$ for comparable P-T-time conditions. Conversely, if negligible water is lost to the assembly, and no iron is lost to the noble metal capsule, the $f\text{O}_2$ is simply a function of the initial $\text{Fe}^{3+}/\text{Fe}^{\text{tot}}$ (e.g. Kagi *et al.*, 2005). In general, we find that the calculated ferric iron components in MORB and AOC runs are systematically different, which suggests that the $f\text{O}_2$ is at least partly controlled by initially different $\text{Fe}^{2+}/\text{Fe}^{3+}$. Since we cannot exclude that the initial $f\text{O}_2$ was modified during the experimental runs, we consider the initial bulk $\text{Fe}^{3+}/\text{Fe}^{\text{tot}}$ defines a lower $f\text{O}_2$ limit ($\sim\text{QFM}$ for MORB, $>\text{QFM}$ for AOC, discussed above), and $\text{NNO}+2(\pm 1)$ an upper limit.

Analytical Techniques

1
2
3
4
5
6
7
8
9
10
11
12
13
14
15
16
17
18
19
20
21
22
23
24
25
26
27
28
29
30
31
32
33
34
35
36
37
38
39
40
41
42
43
44
45
46
47
48
49
50
51
52
53
54
55
56
57
58
59
60

Carbon-coated, polished run products were imaged using a Hitachi S-3500N SEM. Major element electron microprobe analysis (EMPA) was performed in Bristol on a five-spectrometer Cameca SX100, with 15 kV acceleration voltage and 15 nA sample current. The 750°C repeat experiment was measured at ETH on a five-spectrometer JEOL 8200 Superprobe, using similar conditions. A focused electron beam was used for minerals; for glasses, a defocused beam, and reduced sample current (4 nA) were used in order to reduce Na loss, with Na being counted first for 5 seconds only. Due to size issues, a focussed beam was applied for the quantification of “fish egg” textured spherules (see below), which are also glassy in nature. These analyses thus likely suffer from loss of volatile elements such as Na₂O, and concomitant passive enrichment in other major elements.

SIMS analysis of trace elements in experimental glasses was performed at the NERC facility at the University of Edinburgh using a Cameca IMS-4f ion microprobe. The following settings were applied: primary beam of 14.5 kV O⁻ ions; 5 nA beam current: ~15 µm diameter beam. NIST SRM 610 glass (Pearce *et al.* 1997) was used to calibrate relative ion yields; all data were ratioed to Si as determined by EMPA. A 75±20 V energy filter was applied to positive secondary ions accelerated at 4.5 keV to reduce transmission of molecular ions. Subsurface inclusions were monitored in a count-rate versus time diagram and excluded from the averaging procedure. Molecular interferences were removed by conventional peak-stripping using in-house ION6 software. Matrix-dependent ion-yield differences between the calibrant (SRM 610) and natural glasses were evaluated by measuring different standards (MPI DING glasses: STHS, T1, ATHO; USGS glasses: GSD, BCR, BIR; standard values are taken from GeoRem: <http://georem.mpch-mainz.gwdg.de>) three times each over 4 days. Calculated Pearson correlation coefficients of calibration

curves obtained from these standards are 0.97 or better (see Supplementary Data file 1), despite the slope of the correlation being offset from unity, similar to what was found by Skora & Bundy (2012). The corrected bulk-rock data measured on the supra-solidus glasses agree well with trace element data given in Devey *et al.* (1994) for the MORB sample, and average Leg46, 396B-#3A basalts for the AOC sample (Bougault & Cambon, 1979; Dungan *et al.*, 1979; Emmermann & Puchelt, 1979) (Table 1).

Trace elements in glasses from the repeat experiment (AOC 750°C) were measured by laser-ablation inductively coupled plasma mass spectrometry (LA-ICP-MS) at ETH Zürich, using a Resonetics excimer laser (193 nm) coupled to a Thermo Element 2 ICP-MS. The following settings were applied: spot size = 30 µm; frequency = 5 Hz; fluency = 3.5 J/cm²; acquisition time = 30 s (blank) & 40 s (peak); standards were NIST SRM 612 (external), Ca (internal), GSD-1G (secondary). Data were reduced using the Sills software (Guillong *et al.*, 2008), and mineral inclusions were excluded from the glass data via inspection of a count-rate versus time diagram.

To verify the consistency of the SIMS and LA-ICP-MS method we re-analysed all AOC experiments by LA-ICP-MS. There is general agreement between both datasets to mostly better than ±20% except for elements with low overall abundances (<0.1 ppm). A comparison of SIMS and LA-ICP-MS analyses for the supra-liquidus runs is given in Supplementary Data file 1. In 800-900°C runs where melt segregation was incomplete the LA-ICP-MS technique encountered problems with numerous sub-surface inclusions. We therefore prefer to report SIMS data wherever possible. Careful inspection of SIMS and LA-ICP-MS data further suggested a minor surface contamination of Ba from sample preparation. Due to the vesicular nature of the glasses, surface contamination can penetrate

1
2
3
4
5
6
7
8
9
10
11
12
13
14
15
16
17
18
19
20
21
22
23
24
25
26
27
28
29
30
31
32
33
34
35
36
37
38
39
40
41
42
43
44
45
46
47
48
49
50
51
52
53
54
55
56
57
58
59
60

230 into the uppermost few μm , which is beyond the sputtering depth of SIMS. For this reason
231 we report LA-ICP-MS Ba concentrations instead, given that the latter method integrates the
232 signal from a much greater depth ($\sim 20\ \mu\text{m}$).

233
234 **RESULTS**

235 **Phase Relations**

236 All experiments but one (Bristol AOC run at 750°C , no garnet) produced an eclogitic
237 residual assemblage (garnet, omphacitic clinopyroxene) along with some minor and
238 accessory phases (e.g. kyanite, epidote, rutile, Fe-Ti oxide). Due to the water-rich nature of
239 these experiments, all run products contain abundant glass (quenched, supra-solidus melt)
240 that often exhibit evidence for the presence of a co-existing vapour phase in the form of large
241 vapour bubbles. These are sometimes decorated with “fish egg” textured spherules, thought
242 to represent the quenched silicate fraction of a vapour phase rich in dissolved silicates (*c.f.*
243 Adam *et al.*, 1997, discussed below in more detail). Melt/fluid segregation towards the top of
244 the capsule occurred in most runs. All phase proportions (Fig. 1 and Table 2) were
245 determined by least squares regression for average compositions of major phases only,
246 recalculated on an anhydrous basis. Water is re-integrated into the mass balance at a later
247 stage (e.g. Klimm *et al.*, 2008). Note that due to the presence of two immiscible fluids
248 (hydrous melt and siliceous vapour), we cannot calculate the H_2O content of the melt phase,
249 because the fraction of the vapour phase is unconstrained. Thus the calculated liquid fraction
250 in Table 2 represents the bulk liquid (melt+vapour), and not just the melt fraction.

251 Mineral textures and phase petrology vary slightly between MORB and AOC run
252 products. Selected SEM images are given in Fig. 2. In general, MORB experiments at 800-

900°C contain phases that tend to be relatively fine-grained (5-20 µm diameter). Garnets are inclusion-poor and chemically homogenous when compared to many other experimental studies. At 1000°C, in contrast, garnets are relatively coarse grained (20-40 µm), inclusion-rich and zoned.

The sub-solidus MORB experiment (800°C) contains garnet, clinopyroxene, kyanite, epidote, quartz/coesite, rutile, and abundant vapour (no melt). Neither apatite nor phengite was observed due to low bulk K₂O and P₂O₅ respectively (Table 1). Glass and additional garnet replace quartz/coesite, kyanite and some clinopyroxene in the 850°C experiment. Iron-Ti oxide also appears above the solidus. Importantly, epidote remains present above the solidus and does not change in composition to allanite (REE-rich epidote-group mineral) as observed in the doped experiments of Klimm *et al.* (2008). Glasses at 850-900°C exhibit two distinct types of vesicles: microvesicles (~sub- to 1 µm) and large (~10-100 µm), irregular vesicles that may or may not contain “fish eggs.” Microvesicles are common in quenched glasses in water-rich experiments (e.g. Klimm *et al.*, 2008) and are typically ascribed to the fact that the maximum amount of water that can be quenched into room temperature glasses is only 8-10 wt.% (e.g. McMillan & Holloway, 1987), whereas the solubility of water in melts at run conditions is significantly higher (>35 wt % at $P \geq 4$ GPa, e.g. Kessel *et al.*, 2005b). The second, larger set of vesicles is thought to represent a siliceous vapour phase that co-existed with melt at run conditions, exsolving the silicate fraction upon quench to form “fish eggs.” At 1000°C epidote and rutile melted out, but a variety of quench crystals (phengite and other, unidentified, very small phases) are present. In addition, there is no textural evidence for an additional vapour phase at 1000°C.

1
2
3
4
5
6
7
8
9
10
11
12
13
14
15
16
17
18
19
20
21
22
23
24
25
26
27
28
29
30
31
32
33
34
35
36
37
38
39
40
41
42
43
44
45
46
47
48
49
50
51
52
53
54
55
56
57
58
59
60

275 Major phases in AOC run products at 800-1000°C are typically much coarser-grained
276 (20-80 μm). Minor phases (e.g. rutile, etc.) are fine-grained (5-20 μm). The coarse-grained
277 garnets are often inclusion-rich, and exhibit typical growth zoning. In contrast, the AOC
278 750°C repeat experiment exhibits many small garnets due to the presence of garnet seeds in
279 this run (Fig. 2). In clinopyroxenes, we find that omphacitic rims often overgrow smaller,
280 Na-poor cores, which are likely magmatic relicts, given that their compositions are similar to
281 those in the ODP report of Sato *et al.* (1979). Igneous clinopyroxenes apparently provided
282 nuclei for high-pressure experimental clinopyroxenes. Fortunately, relict clinopyroxene
283 cores in AOC experiments are of minor volumetric abundance compared to their omphacitic
284 rims.

285 One AOC experiment (Bristol, 750°C) contains clinopyroxene, staurolite, phengite
286 epidote, quartz/coesite, rutile, Fe-Ti oxide, apatite and vapour with abundant “fish eggs”.
287 Garnet and clear evidence for melt are lacking. Repeating this experiment at ETH with
288 garnet seeds produced abundant garnet, as growth rims (Fig. 2), clinopyroxene, glass and
289 rutile, as well as fine-grained epidote-clinozoisite; we interpret this repeat run as a more
290 close approach to equilibrium (see detailed discussion below). Changes in phase
291 assemblages and proportions are fairly consistent with increasing temperature. Glass, garnet,
292 clinopyroxene and some trace phases (rutile, Fe-Ti oxide, epidote, kyanite) remain present
293 up to 900°C. Apatite is either melted out above the solidus or too small to observe. Similar to
294 MORB experiments, a vesicular glass coexists with an additional fluid phase (large vesicles
295 with or without fish-eggs) at 750-850°C. The 900°C run product visually differs from the
296 850°C run product by having a slightly increased glass fraction and no clear evidence for the

second fluid phase. At 1000°C glass, with quench crystals, is abundant (>40%), and epidote, rutile and kyanite are melted-out.

Approach to equilibrium

It is straightforward to show that near-equilibrium conditions were reached with our MORB starting material, which was a glassy basalt with less than 10% olivine and minor plagioclase and spinel. All igneous phases were fully replaced by an eclogitic assemblage (garnet, clinopyroxene, other minor and accessory phases, as well as melt above the solidus), which is relatively homogeneous and comparable to other studies (Supplementary Data (SD) file 2). The AOC run products exhibit broadly similar phase assemblages, as well as melt and mineral compositions that are comparable to MORB run products (SD file 2). This suggests that near-equilibrium conditions were reached in all but a single Bristol AOC run at 750°C, which lacked garnet. The failure of garnet to nucleate can be explained by its sluggish nucleation kinetics in high-pressure experiments. This conclusion is consistent with the presence of garnet overgrowth rims in the garnet-seeded, repeat experiment at ETH Zürich, indicating that garnet belongs to the high-pressure sub-solidus assemblage at 3 GPa, 750°C. Other AOC run products also exhibit some features indicative of local disequilibrium, including growth zoning in garnet as well as small relict igneous clinopyroxenes that are surrounded by omphacite. Mass balance and all interpretations below are based on volumetrically dominant garnet and clinopyroxene rim compositions, because they will be in equilibrium with the co-existing phases.

Phase chemistry - major elements

1
2
3
4
5
6
7
8
9
10
11
12
13
14
15
16
17
18
19
20
21
22
23
24
25
26
27
28
29
30
31
32
33
34
35
36
37
38
39
40
41
42
43
44
45
46
47
48
49
50
51
52
53
54
55
56
57
58
59
60

Experimental glasses and silicate minerals are relatively homogenous: in most cases major elements have 1σ of $<10\%$ relative; minor elements have $1\sigma = 10-50\%$ relative (Table 3). Notable exceptions are glasses in the MORB 850°C experiment, hampered because the small melt pools are not well interconnected, as well as both 1000°C experiments due to the development of abundant quench crystals. In the latter cases, however, the average of a large number of analyses should approximate the equilibrium composition, despite large standard errors. *Glasses* are generally rich in SiO_2 , Al_2O_3 , CaO and alkalis, and poor in MgO and FeO . Low EMPA totals as well as the microvesicular nature of quenched glasses imply that they contain significant H_2O . “Fish egg” textured spherules also appear glassy in nature and are broadly granitic in composition (see Table 4).

The MORB partial melts are peraluminous and tonalitic in composition (according to the classification scheme of Barker, 1979) just above the solidus, trending towards a more metaluminous composition at higher temperatures (Fig. 3). The AOC partial melts are also peraluminous, but trondhjemitic. Like MORB melts, they become metaluminous at higher temperatures, and further change their composition at $T \geq 900^\circ\text{C}$ to become tonalitic (Fig. 3). Magnesium oxide and FeO contents of all glasses are uniformly low, although both elements increase slightly at higher temperatures (Fig. 4). The Mg\# decreases slightly between 750 and 1000°C from around 0.5-0.6 to around 0.4-0.5 in both experimental sequences (Table 3). Such compositions are fully consistent with other published studies on partial melts of a basaltic composition with excess water (range: 5-25 wt.%) at broadly similar P-T (Pressure-Temperature) conditions (e.g. Ryabchikov *et al.*, 1996 (E3 composition); Prouteau *et al.*, 2001 (3 GPa subset); Kessel *et al.*, 2005b (4 GPa, 900-1000°C subset); Klimm *et al.*, 2008; Prouteau & Scaillet, 2013) (SD file 2). Remaining small discrepancies between all these

studies can be related to differences in bulk composition, fO_2 , pressure (range: 2.5-4 GPa) and the degree of melting as a consequence of different starting H_2O contents.

Major element compositions of minerals are given in SD file 3. The method of Droop (1987) was used to estimate Fe^{3+} contents for garnet and clinopyroxene and stoichiometric considerations are used for all other minerals. Garnets in MORB and AOC run products are compositionally similar at similar temperatures, being rich in almandine (25-40%), pyrope (30-44%) and grossular (23-30%), but poor in spessartine (<1%) and andradite (1-6%). Where zoning occurs, garnets display increasing pyrope and decreasing almandine from core to rim. A small but noticeable difference between the experimental sequences lies in the calculated andradite component, which tends to be lower at lower temperatures (800-900°C) in MORB (1-2.7%) than in AOC (1.7-6.5%), in keeping with higher initial Fe^{3+}/Fe^{tot} in AOC. In contrast, calculated andradite components are consistently higher (5.2-7.5%) at 1000°C. With increasing temperature, the pyrope component increases mostly at the expense of almandine, gradually changing the Mg# from around 0.4 to around 0.6. Garnet Mg# hence mirrors the behaviour of melts, which become more iron-rich at higher temperatures. Other minor elements observed in garnet include TiO_2 , which increases slightly with increasing temperature in the presence of rutile. Experimental garnet compositions and chemical trends with temperature are fully consistent with other experimental studies (see SD file 2).

Clinopyroxenes are all omphacites, and are less chemically variable than garnet. A comparison to other studies is given in SD file 2. They exhibit a significant 'quadrilateral' (QUAD) Ca-Mg-Fe component (74-76% in MORB, 62-66% in AOC), a jadeite component (18-24% in MORB, 23-31% in AOC), and a small, but significant, calculated acmite component (2-8% in MORB, 3-11% in AOC). The acmite component is likely a maximum

1
2
3
4
5
6
7
8
9
10
11
12
13
14
15
16
17
18
19
20
21
22
23
24
25
26
27
28
29
30
31
32
33
34
35
36
37
38
39
40
41
42
43
44
45
46
47
48
49
50
51
52
53
54
55
56
57
58
59
60

estimate due to the possible presence of a small Ca-eskolaite component (e.g. Konzett *et al.*, 2007). The relict igneous cores in AOC (750-900°C) are ~90% QUAD in composition, with a relatively high acmite component (4.5-7.5%), and significantly higher Ti compared to high-pressure, omphacite rims.

Minor phases that were observed include kyanite, which is relatively pure Al_2SiO_5 , although a small quantity of iron (likely Fe_2O_3) is detectable (~3 wt % in MORB; ~4 wt % in AOC). Epidotes are epidote-clinozoisite solid solutions, containing approximately 8-10 wt % total iron, which should be mostly Fe_2O_3 . The SiO_2 phase that occurs in sub-solidus runs should be coesite, although this is hard to distinguish from quartz in our run products, based on textural criteria alone. Iron–Ti oxides of the ilmenite–hematite solid solution series are present in almost all runs, displaying a significant hematite component (~55-75 mol%), and a small Al_2O_3 component (~1-4 mol%). Rutile, which contains some ferric iron (~2-7 mol%), is present in all runs below 1000°C. Apatite was found in a single run only (750°C; AOC without melt and garnet), suggesting that this is the main phase that carries P_2O_5 down to sub-arc depth in phosphate-rich basalts, until it is melted out above the solidus.

Glass chemistry - trace elements

With increasing temperature several systematic variations in glass chemistry are observed. Concentrations are given in Table 5 and plotted (normalised to Primitive Upper Mantle [PUM]) in Fig. 5 and against temperature in Fig. 6. The AOC experiments provide the most complete dataset in terms of temperature evolution (750-1000°C), but some insights can also be derived from the MORB data at 900 and 1000°C. In general, fluid-mobile elements such as Cs, Rb, Ba, Sr and Li are always enriched in the partial melts. Other elements such as U,

1
2
3 389 Zr, Hf, and V are also moderately enriched. Elements such as Nb, Ta, LREE and Th are
4
5
6 390 relatively depleted at $T \leq 900^\circ\text{C}$. Heavy REE, Y and Sc are relatively depleted at all
7
8 391 temperatures. Different element groups behave differently with increasing temperature, e.g.
9
10 392 HREE, Y and Sc concentrations increase with increasing temperature, in contrast to most
11
12 393 fluid-mobile elements. The different trace element patterns are explained in more detail
13
14 394 below.
15
16
17
18 395

19 20 396 **DISCUSSION**

21 22 397 **Location of the Solidus**

23
24 398 Our experiments place constraints on the 3 GPa, H_2O -saturated solidus of ocean floor basalt,
25
26 399 which is shown to be sensitive to bulk K_2O content. Our AOC experiments (~ 0.25 wt.%
27
28 400 K_2O) produced glass (+ garnet, clinopyroxene, minor phases) at 750°C only in the
29
30 401 experiment that contained garnet seeds. The other experiment at 750°C contained “fish eggs”
31
32 402 instead of melt, together with clinopyroxene, staurolite (for reasons detailed in Skora &
33
34 403 Blundy (2010) staurolite is likely metastable relative to garnet and kyanite), phengite,
35
36 404 quartz/coesite and minor phases. It is tempting to conclude that the lack of melt in the latter
37
38 405 750°C experiment is due to garnet nucleation problems and related overall disequilibrium.
39
40 406 However, the most widely proposed H_2O -saturated melting reaction for K-bearing MORB
41
42 407 and sediment is quartz/coesite + phengite + clinopyroxene + H_2O = melt + garnet (e.g.
43
44 408 Hermann & Green, 2001; Hermann & Spandler, 2008; Schmidt, 1996; Skora & Blundy,
45
46 409 2010). As garnet is a product of melting, it is unlikely that the lack of garnet should inhibit
47
48 410 melting. Alternatively, melting in K-bearing AOC may start at temperatures that are very
49
50
51
52
53
54
55 411 close to 750°C , and small calibration-related P-T discrepancies between Bristol and ETH
56
57
58
59
60

1
2
3 412 Zürich (e.g. due to different thermocouple types) may be responsible. For basalt with 0.14
4
5 413 wt.% K₂O and excess water, Lambert & Wyllie (1972) determined a 3 GPa solidus
6
7 414 temperature of ~750°C, whereas Schmidt & Poli (1998) located their solidus at ~730°C for
8
9 415 MORB with 0.49 wt % K₂O. Thus, regardless of whether the lack of melt in one 750°C
10
11 416 experiment is due to P-T uncertainties or due to disequilibrium, we conclude that melting in
12
13 417 K-rich AOC starts at $T \approx 750^{\circ}\text{C}$, in keeping with previous studies.
14
15
16

17 418 Quenched silicate melt formed only above 800°C in the MORB experiments, placing
18
19 419 the 3 GPa solidus for a starting material with only 0.04 wt.% K₂O between 800 and 850°C
20
21 420 ($T=825\pm 25^{\circ}\text{C}$). In theory, no phase other than phengite is capable of hosting appreciable
22
23 421 potassium in an eclogitic assemblage at around 3 GPa, a fact confirmed by analyses of
24
25 422 silicate minerals in this run (SD file 3). Sub-solidus phengite, however, was not observed.
26
27 423 Possibly phengites were never found because 0.04 wt % initial K₂O equates to just ~0.4
28
29 424 vol% phengite. Alternatively appreciable potassium was dissolved in the siliceous fluid
30
31 425 (quenched as “fish eggs”) at near-solidus conditions (Table 4), effectively stripping out all
32
33 426 the potassium from the solid assemblage. We note that the K-free, water-rich experiments of
34
35 427 Kessel *et al.* (2005b) determined a 4 GPa solidus temperature of $875\pm 12^{\circ}\text{C}$. Assuming a
36
37 428 constant offset between K-bearing and K-free MORB at 3 and 4 GPa, the solidus estimates
38
39 429 of Kessel *et al.* (2005b) and Lambert & Wyllie (1972) can be extrapolated to a 3 GPa, K-free
40
41 430 MORB solidus temperature of around 850°C, consistent with our experimental results. The
42
43 431 melting reaction, however, differs slightly from that given in Kessel *et al.* (2005b). We find
44
45 432 that glass and garnet replace quartz/coesite, kyanite and some clinopyroxene in the 850°C
46
47 433 experiment, suggesting an initially incongruent melting reaction of the form: quartz/coesite +
48
49 434 kyanite + clinopyroxene + H₂O = melt + garnet. Kessel *et al.* (2005b) propose instead a
50
51
52
53
54
55
56
57
58
59
60

1
2
3 435 congruent melting reaction of the form: clinopyroxene + garnet = melt. To what extent the
4
5 436 discrepancies relate to differences in pressure or bulk-rock composition remains uncertain at
6
7
8 437 this stage, but it is evident that both reactions would occur at somewhat similar temperatures
9
10 438 in subduction zones.

11
12
13 439 The question persists as to whether AOC and MORB can melt at Wadati-Benioff
14
15 440 zone depths (approx. 75-135 km, average \approx 105 km, Syracuse *et al.*, 2010), provided that
16
17 441 sufficient H₂O can be added via the breakdown of hydrous minerals such as serpentine or
18
19 442 chlorite in deeper portions of the slab. Recent results in thermal modelling (e.g. Syracuse *et*
20
21 443 *al.*, 2010; van Keken *et al.*, 2011) predict slab-top temperatures of around 750-850°C in
22
23 444 most subduction zones at 2.5-4.5 GPa (e.g. Lesser Antilles), with some offset towards higher
24
25 445 temperatures (850-950°C, e.g. Nicaragua; Guatemala). These temperatures drop off in the
26
27 446 lower parts of the subducted column, and are approx. 100-300°C lower than slab-top
28
29 447 temperatures at the bottom of a 7 km thick basaltic crust (e.g. van Keken *et al.*, 2011).
30
31 448 Combined with our experimentally-derived, H₂O-saturated solidus temperatures, these
32
33 449 results suggest that only the top part of the basaltic crust can melt, if present as altered
34
35 450 oceanic crust with elevated K₂O contents. K-poor MORB is less likely to melt except in the
36
37 451 hottest subduction zones. Melt fractions of oceanic basalts will be significantly lower
38
39 452 compared to those of overlying, K-rich marine sediments (e.g. Schmidt *et al.*, 2004).
40
41
42
43
44
45
46 453

454 Nature of experimental fluids

455 The second critical end-point (SCEP) is defined in P-T space by the intersection of the melt-
456 vapour critical curve and the H₂O-saturated solidus (see e.g. Hermann *et al.*, 2006; Manning,
457 2004). The conventional designation of solidus, melt and vapour is lost at pressures
458 exceeding the SCEP because melt and H₂O are fully miscible supercritical fluids.
459 Experimental studies have come to different conclusions concerning the position of the
460 SCEP in the system basalt-H₂O (or more correctly the system basalt-derived partial melt-
461 H₂O). Kessel *et al.* (2005b) used topological criteria to estimate the SCEP in K-free basalt to
462 lie between 5 and 6 GPa. This is close to the position of the SCEP in K-MORB as estimated
463 by Schmidt *et al.* (2004) using textural evidence. On the basis of extrapolation from the
464 haplogranite critical curve to the H₂O-saturated basalt solidus, Klimm *et al.* (2008) proposed
465 that the SCEP lies at ~2.5 GPa in K-MORB. This discrepancy raises the question as to
466 whether MORB/AOC-derived fluids beneath arcs are supercritical in nature, or not.

467 In our experimental charges, MORB glasses at 850-900°C and AOC glasses at 800-
468 850°C clearly exhibit two distinct types of vesicles: (a) microvesicles that are evident in all
469 glass pools and (b) large, irregular vesicles that are also present in glass pools and that may
470 or may not contain “fish eggs.” Microvesicles in glasses (a) are commonly interpreted to
471 represent vapour-exsolution upon quench (e.g. Klimm *et al.*, 2008). Larger vesicles (b) are
472 interpreted to represent an additional vapour phase that co-existed with hydrous melt
473 (=quenched glasses) at run conditions. The “fish eggs” are suggested to represent the
474 siliceous fraction that was dissolved in the vapour phase at run conditions. Our textural
475 evidence argues for two fluid phases at near-solidus conditions, hydrous melt + siliceous
476 vapour (Fig. 7). Our experimental data thus suggest sub-critical conditions and place the

1
2
3 477 SCEP at pressures greater than 3 GPa in both MORB- and AOC-derived fluids, consistent
4
5 478 with Kessel *et al.* (2005b) and Schmidt *et al.* (2004). Above 900°C (MORB) and 850°C
6
7 479 (AOC), clear evidence for an additional vapour phase (\pm “fish egg” textured spherules)
8
9 480 disappears, suggesting that complete fluid-melt miscibility (supercritical behaviour) may
10
11 481 occur in response to increasing temperature and changing melt composition. We further offer
12
13 482 a possible explanation for the discrepant result of Klimm *et al.* (2008) in SD file 4.
14
15
16
17
18
19

20 484 **Trace elements in fluid and melt**

21
22 485 It is well known that the behaviour of trace and minor elements in the glass with increasing
23
24 486 temperature is a direct consequence of the residual mineralogy, specifically the phases that
25
26 487 control the budget of those elements (e.g. rutile: Klemme *et al.*, 2002). For elements that
27
28 488 lack a residual host phase the concentration in the glass will decrease with temperature,
29
30 489 whereas for elements with a ubiquitous host phase, element concentrations will increase with
31
32 490 temperature. For elements whose host phase becomes exhausted over the melting interval the
33
34 491 concentration in the glass will attain a maximum at the point of phase exhaustion. Naturally
35
36 492 all trace element contents attain those of the bulk starting material at the liquidus
37
38 493 temperature. A complexity arises for those elements that strongly partition into a separate
39
40 494 vapour phase, i.e. for sub-critical conditions. In that case the exhaustion of the vapour phase
41
42 495 upon attainment of criticality will lead to a maximum in glass concentration in much the
43
44 496 same way as exhaustion of a solid residual phase.
45
46
47
48
49

50 497 Titanium, Nb and Ta show a continuous increase in concentration with temperature,
51
52 498 with the same trends observed for MORB and AOC, consistent with the persistence of
53
54 499 residual rutile up to 900°C and Fe-Ti-oxide thereafter (Fig. 6). Note that Fe-Ti oxides are
55
56
57
58
59
60

unlikely to host significant quantities of Nb and Ta because of the significant hematite component (*c.f.* Skora & Blundy, 2010). In AOC glasses Zr (and Hf) shows a marked peak in concentration at around 900°C (Fig. 6). We lack the resolution in MORB glasses to establish if there is a maximum or not. The tendency of Zr and Hf to attain maxima at intermediate temperatures in AOC suggests the exhaustion of zircon at ~900°C during melting, although zircon was never positively identified in our experiments due to low bulk Zr. Scandium, V, Y and HREE also show an overall increase in the glass from 750-1000°C due to the persistence of garnet and, to a lesser extent, omphacite across the melting interval (Fig. 6). The slightly complex behaviour of Sc and V may reflect competition between garnet and omphacite and their changing proportion in the residue with increasing temperature. Light REE abundances are extremely low (<1-3 ppm total LREE) in all glass-bearing experiments on MORB and AOC, except at the highest temperature when their concentrations increase sharply (Fig. 6). This behaviour is a consequence of residual epidote, which is known to host these elements (e.g. Frei *et al.*, 2004) and approaches exhaustion at the highest run temperatures. The 800°C AOC run has higher LREE than either of the adjacent runs. This behaviour is suggestive of less epidote in this run, which may be a result of a small inter-run variability in fO_2 , which influences epidote stability and proportion through control of Fe^{3+} . Uranium and Th concentrations are also very low (<0.3 ppm) in all experimental glasses, and consequently subject to high analytical uncertainty, making trends hard to discern. Nonetheless Th clearly increases with temperature until $T = 900^\circ C$, similar to Ce (Fig. 6). Again, epidote appears responsible for this behaviour.

The LILE K, Ba, Cs, Rb, Sr and Li in glasses show variable behaviour (Fig. 6). Caesium decreases steadily with temperature in the AOC and MORB experiments,

indicative of behaviour as an incompatible element with no residual host phase. Potassium and Rb show broad maxima at around 800-850°C in AOC, and 900°C (K only) in MORB. Barium in AOC shows a maximum at 850°C, whereas Li shows a broad maximum at 850-900°C. Strontium shows a maximum between 900 and 1000°C in both sets of experiments. Finally, Na shows a maximum in MORB at 900°C, but rather irregular behaviour in AOC. With the possible exceptions of Sr in epidote (SD file 5) and Na and Li in omphacite (e.g. Hermann 2002a), none of LILE have a residual host phase; phengite, a potential host for K and Ba is exhausted above the solidus of MORB and AOC. Thus the maxima that the LILE display cannot be ascribed to exhaustion of a solid phase. However, it is striking that the various maxima displayed by LILE roughly correspond to the transition from sub-critical to super-critical behaviour (850-900°C in AOC, 900-1000°C in MORB), as evidenced texturally, suggesting a role for fluids in LILE transport. In much the same way as exhaustion of a solid phase produces maxima for other trace elements so the exhaustion of the fluid phase on crossing the solvus into super-critical behaviour can lead to maxima in the concentrations of elements that possibly partition into the fluid. In detail the temperature at which the maximum occurs over the transition to supercritical behaviour will reflect the strength of partitioning into the fluid. Thus our data suggest that fluid-melt partitioning increases in the order Cs<Rb<K<Ba in AOC. The behaviour of Na in this sequence is unclear. This is an interesting insight into LILE fluid partitioning, but dedicated experiments would be required to quantify it.

544 **Allanite versus epidote and the behaviour of light rare earth elements**

545 The behaviour of LREE+Th in our experimental glasses is controlled by the presence of
546 residual epidote. Light REE abundances are extremely low (<1-3 ppm total LREE, Fig. 8) in
547 all glass-bearing experiments on MORB and AOC, except at the highest temperature when
548 epidote is exhausted. Epidote forms a solid solution with allanite, indicating a demonstrable
549 ability to accommodate LREE in its structure (e.g. Frei *et al.*, 2003). Analyses of epidote in
550 our run products show elevated LREE, in one case readily analysable by EMPA (SD file 5).
551 For example in a run on AOC at 900°C epidote contains 1000±300 ppm Ce, 400±100 ppm
552 La, and 900±300 ppm Nd. The corresponding epidote-melt partition coefficients are:
553 $D_{La} \approx 1500 \pm 600$, $D_{Ce} \approx 1200 \pm 400$, $D_{Nd} \approx 700 \pm 300$ (SD file 6). The observed concentrations of
554 Σ LREE (La-Sm) are much lower than those required for allanite solubility (Fig. 8),
555 confirming that this mineral was absent from our experiments in contrast to those of
556 Hermann (2002a) and Klimm *et al.* (2008). We attribute this key difference to the relatively
557 high doping levels of LREE used in those studies. In fact the LREE partition coefficients
558 between epidote and melt given above are higher than those for allanite at 900°C and 2.5
559 GPa (Klimm *et al.*, 2008) by a factor of ~2.

560 It is logical to conclude that doping with LREE in the experiments of Hermann
561 (2002b), Kessel *et al.* (2005a) and Klimm *et al.* (2008), where allanite was found to be the
562 principal carrier for LREE+Th, simply pushed the composition of the allanite-epidote solid
563 solution to the high LREE end-member, thereby increasing the overall level of LREE+Th in
564 the glasses in the doped experiments. Additional evidence for the stability of allanite versus
565 epidote can be drawn from field examples. Although allanites are found in some (ultra) high-
566 pressure ((U)HP) terrains, they are typically restricted to REE-enriched rocks with alkaline

1
2
3
4 567 affinities (as opposed to N-MORB), or Fe-gabbros (e.g. Hermann, 2002b; Spandler *et al.*,
5
6 568 2003; Tribuzio *et al.*, 1996). These rock types are not representative of average oceanic
7
8 569 basaltic crust and indeed, epidote/zoisite is much more common in exhumed (U)HP terrains
9
10 570 (Enami *et al.*, 2004). Note in that context that UHP terrains most often represent the un-
11
12 571 molten, sub-solidus protolith of subducted crust, and allanite only forms above the solidus
13
14 572 according to Klimm *et al.* (2008) (reaction: epidote = allanite + melt). Our experimental
15
16 573 study suggests however that epidote would not change its composition appreciably above the
17
18 574 solidus.

19
20
21
22 575 We conclude that the control on LREE contents of subduction zone melts of basalt is
23
24 576 still an epidote-group mineral, but one much poorer in LREE than allanite. A simple test of
25
26 577 this proposal is to use the solubility model of Klimm *et al.* (2008), but with the epidote
27
28 578 compositions determined in our experiments (Fig. 7). These have considerably lower mole
29
30 579 fractions of allanite (X_{all}), which leads to much lower levels of LREE in the melt according
31
32 580 to equation (9) in Klimm *et al.* (2008). We use the epidote from the AOC 900°C run with the
33
34 581 LREE contents given in SD file 5. In this run $X_{\text{all}} \approx 0.008$, assuming ideal mixing this would
35
36 582 equate to a LREE content in melts 125 times lower than if pure allanite were present in the
37
38 583 residue. Inspection of Fig. 8 shows that this is indeed the case for this run: at 900°C Klimm
39
40 584 *et al.* (2008) find $X_{\text{all}} \approx 0.4$ and ΣLREE (La-Sm) in the melt is 168 ppm, whereas we have
41
42 585 $X_{\text{all}} = 0.008$ and $\Sigma\text{LREE} = 2.7$ ppm, i.e. X_{all} is 53 times lower and ΣLREE 62 times lower in
43
44 586 our experiment as compared to Klimm *et al.* (2008). The close correspondence between the
45
46 587 observed X_{all} and melt LREE content in our experiments and those of Klimm *et al.* (2008)
47
48 588 lends strong support to the notion that epidote-group minerals limit the flux of LREE from
49
50 589 subducted basalt to the mantle wedge at temperatures below 900°C.
51
52
53
54
55
56
57
58
59
60

1
2
3
4
5
6
7
8
9
10
11
12
13
14
15
16
17
18
19
20
21
22
23
24
25
26
27
28
29
30
31
32
33
34
35
36
37
38
39
40
41
42
43
44
45
46
47
48
49
50
51
52
53
54
55
56
57
58
59
60

In order to employ the allanite solubility approach to better understand basalt-derived fluxes of LREE+Th (e.g. Plank *et al.*, 2009), we need a thermodynamic model of the allanite-epidote solid solution. In addition, we need to constrain the bulk-rock and fO_2 control on epidote-zoisite solid solutions and their respective stability fields. For example, the stability field of the zoisite end-member in MORB does not extend much beyond 2.5 GPa / 800°C or 3 GPa / 700°C (e.g. Poli *et al.*, 2009; Schmidt & Poli, 1998). Our experiments reveal that Fe^{3+} -bearing epidote may well be stable at much higher temperatures at 3 GPa. Hence X_{all} in epidote has the potential to vary significantly. It is also known that partition coefficients of LREE+Th, and possibly U, vary as a function of the epidote-zoisite solid solution (see e.g. Frei *et al.*, 2003, 2004; Martin *et al.*, 2011). In the absence of any such data our experiments provide useful first constraints, demonstrating that negligible basalt-derived LREE+Th concentrations enter the arc basalt source region. Unless slab-top temperatures are much higher than existing models would suggest, LREE+Th enrichment in arc magmas must therefore originate from the sedimentary veneer.

Implications for arc basalt trace element geochemistry

Our experiments have a number of implications for the chemistry of the basalt-derived component added to the mantle wedge source of arc basalts. Although the tripartite model of the arc magma source reviewed by Elliott (2003) (Fig. 9) advocates an aqueous fluid as the key-transporting agent of trace elements from the basaltic portion of the slab to the wedge, it is instructive to evaluate the potential for basalt-derived melts to affect the required chemical signal. Note that although at super-critical or near super-critical conditions the distinction between fluid and melt disappears, there is still a relationship between total solutes in the

1
2
3
4 613 fluid phase and temperature. At low temperatures, the composition and physical properties
5
6 614 of the fluid phase will resemble an aqueous fluid, whereas at high temperatures it will
7
8 615 resemble a hydrous melt (e.g. Fig. 11 of Hermann & Rubatto, 2014). Thus, our data are
9
10 616 principally also relevant for supercritical fluids that have the physical properties of a hydrous
11
12 617 melt. Our basalt-derived melts approximate the composition of the total subduction
13
14 618 component only in the case of sediment-starved arcs; sediment-derived melts will have quite
15
16 619 different trace element chemistries because of their different bulk compositions, leading to
17
18 620 different residual assemblages at high pressure, and initial trace element inventories. For this
19
20 621 reason we compare directly the trace element composition of our experimental melts to
21
22 622 basaltic arc lavas whose subduction component is thought to be dominated by material from
23
24 623 the mafic crust (e.g. Tonga, Izu-Bonin, some Mariana islands; Elliott, 2003). Since our
25
26 624 experimental starting materials were undoped, it is possible, for the first time, to make direct
27
28 625 inferences about the melt flux from subducted basalt as a function of temperature based on
29
30 626 analyses of trace elements in quenched experimental glasses.
31
32
33
34
35
36
37
38

39 628 *Trace element contribution*

40
41 629 Primitive upper mantle-normalised trace element patterns for melts derived from MORB and
42
43 630 AOC exhibit several striking features (Fig. 5). First, the overall concentrations of trace
44
45 631 elements, relative to PUM, increase with increasing temperature, although fractionation
46
47 632 between adjacent elements decreases with increasing temperature. Thus the most “spiky”
48
49 633 trace element patterns are observed at the lowest temperatures. Second, the only elements
50
51 634 with concentrations significantly higher (factor >3) than PUM at all temperatures, and
52
53 635 therefore able to significantly modify the trace element chemistry of the mantle wedge, are
54
55
56
57
58
59
60

1
2
3
4
5
6
7
8
9
10
11
12
13
14
15
16
17
18
19
20
21
22
23
24
25
26
27
28
29
30
31
32
33
34
35
36
37
38
39
40
41
42
43
44
45
46
47
48
49
50
51
52
53
54
55
56
57
58
59
60

the fluid mobile elements (e.g. Cs, Rb, K, Ba, Sr, and U). This is consistent with their enrichment even in sediment-starved arcs (e.g. Tonga, Izu-Bonin, some Mariana islands). Zirconium, Hf and Li are also surprisingly enriched in our partial melts (see below). Titanium, Nb and Ta enrichments only exceed a factor of 3 at the highest temperatures studied ($>900^{\circ}\text{C}$). REE are lower than $3\times\text{PUM}$ except at 1000°C .

Sediment-starved arcs typically have low concentrations of many incompatible elements when compared to sediment-rich arcs, and exhibit low La/Sm, high Ba/Th, as well as Sr isotope ratios consistent with contributions from an altered MORB source. Elliott (2003) showed that the Ba/Th ratio of the basalt-derived component is in excess of 1000 with a $(\text{La/Sm})_{\text{PUM}}$ of around 1 (Fig. 5). This special characteristic of the arc geochemical signature has been traditionally ascribed to a “fluid” phase from subducted mafic oceanic crust. However, similar characteristics are observed in our melts at $800\text{--}850^{\circ}\text{C}$ from an AOC source in which residual epidote is present (retaining Th) but phengite (retaining Ba) is absent. The same is likely to be true for the 750°C AOC experiment, but exact Ba/Th and $(\text{La/Sm})_{\text{PUM}}$ could not be determined because Th, La and Sm were below detection. At higher temperatures the increased Th content, enabled by the progressive breakdown of epidote, as well as increased melt fractions, reduce Ba/Th significantly (Fig. 5). At lower (sub-solidus) temperatures, the presence of residual phengite will retain Ba and reduce Ba/Th in the fluid. This is readily apparent from the 650°C , 3 GPa sub-solidus fluid analyses of Green & Adam (2003). At 700°C the Ba/Th of sub-solidus fluids approaches those measured in our supra-solidus experiments, likely because the solubility of phengite and other silicates is enhanced in near-solidus fluids (e.g. Manning *et al.*, 2010). (Note in that context that Green & Adam (2003) used a doped starting material. Whether the absolute

659 Ba/Th values given in Green & Adam (2003) truly approximate nature requires undoped
660 experiments).

661 Our results suggest that the Ba/Th and $(\text{La/Sm})_{\text{PUM}}$ characteristics of the “fluid”
662 component can be delivered by a wet melt of basalt (Fig. 9). Further complexity in Ba is
663 introduced across the transition from sub- to super-critical behavior, as noted above.
664 However, by far the greatest influence on Ba/Th ratios of melts is the presence or absence of
665 phengite and epidote. Epidote stability is complex, as discussed above. Phengite stability, in
666 turn, is primarily a function of bulk K_2O and H_2O , given that there is a strong relationship
667 between X_{phengite} (the only host of K_2O at sub-arc conditions), H_2O and the degree of melting
668 (e.g. Schmidt *et al.*, 2004; Skora & Blundy, 2010). In our water-rich experiments, the Ba/Th
669 ratio of melts supplied by the slab basalt end-member is controlled primarily by temperature,
670 with the highest ratios being generated in the narrow window between exhaustion of
671 phengite (at the solidus) and exhaustion of epidote (melted out above the solidus, at approx.
672 900°C). This window lies between $750\text{--}800$ and 850°C (Fig. 9).

673 It is also worth noting that our sub-solidus, K-poor MORB run product contains
674 epidote but no phengite, likely because the very low initial potassium content is fully
675 dissolved in the fluid phase (discussed above). If this is generally the case, then Ba lacks a
676 host in the sub-solidus mineral assemblage of subducted MORB at these conditions and may
677 also be concentrated in the fluid phase. In contrast, Th will be retained by residual epidote
678 and so fluids equilibrated with K-poor MORB at sub-solidus conditions may also have high
679 Ba/Th ratios. It is therefore conceivable that fluids derived from lower parts of the subducted
680 basalt, and equilibrated with unaltered MORB at sub-solidus conditions, as well as partial
681 melt from the uppermost AOC are jointly responsible for the high Ba/Th ratios observed in

1
2
3
4
5
6
7
8
9
10
11
12
13
14
15
16
17
18
19
20
21
22
23
24
25
26
27
28
29
30
31
32
33
34
35
36
37
38
39
40
41
42
43
44
45
46
47
48
49
50
51
52
53
54
55
56
57
58
59
60

sediment starved arcs. Our experiments show how effective epidote can be at keeping Ba/Th high and La/Sm low.

The tendency of our melts to show elevated Zr/Nd (range: 10-1070), Hf/Sm (range: 1-60), and Li/Y (range: 3-80) ratios (Fig. 5) may at first seem paradoxical given that arc basalts do not show positive anomalies for these elements. Using the same compilation as Elliott (2003) for the most mafic Izu-Bonin and Tonga lavas, these ratios are closer to 7 ± 1 (Zr/Hf), 0.6 ± 0.1 (Hf/Sm) and 0.4 ± 0.1 (Li/Y). However, the trace element ratios of the added slab component are only mirrored in arc basalts when the elements of interest are not incorporated significantly into mantle minerals (e.g. Ba/Th). Zirconium, Hf and Li, however, are only modestly incompatible in mantle minerals (pyroxene, olivine). Studies such as that of Stolper & Newman (1994) have quantified the exchange of elements with the mantle wedge and concluded that all but the most incompatible elements are likely to equilibrate with it. Hence, we suggest that Zr, Hf and Li can be significantly modified by equilibration with the mantle wedge, to the extent that they no longer provide a clear insight into slab processes.

Finally we note that melts derived from the basaltic portion of the slab have elevated U/Th ratios. This will lead to isotopic disequilibrium between the activities of ^{238}U and ^{230}Th that will be retained in the melt on timescales less than five half-lives of ^{230}Th (i.e. 350 ky). An activity excess of ^{238}U over ^{230}Th is a characteristic of many sediment-starved arcs (e.g. McDermott & Hawkesworth, 1991). For example, in the Marianas the maximum ^{238}U activity excess over ^{230}Th observed by Elliott *et al.* (1997) and Avanzinelli *et al.* (2012) is ~ 1.6 (also see Elliott, 2003 for a compilation of high ^{238}U activity excess over ^{230}Th). Such a value is consistent with basalt-derived melts generated at 800-850°C from AOC, although

we note that our source normalized U/Th ratios are poorly constrained due to analytical limitations.

CONCLUSIONS

Through a series of experiments conducted at sub-arc P-T conditions (750-1000°C, 3 GPa) in the presence of excess water, we show that the temperature and composition of the down-going oceanic crust (pristine MORB versus AOC) can have a profound effect on the sub-arc phase assemblage and geochemistry, and therefore the resulting slab contribution to arc magma geochemistry. Notably, an order of magnitude elevated potassium content in AOC over MORB shifts the water-saturated basaltic solidus to lower temperature (~750°C AOC, 825±25°C MORB). Just above the solidus, run products texturally indicate the presence of two liquids: an aqueous fluid with quench “fish eggs,” and a vesicular hydrous melt. With increasing temperature, the second vapour phase diminishes and disappears across the solvus. Further experimentation at varying P, X_{H_2O} is needed to constrain the solvi and second critical endpoints for AOC and MORB.

For slab-top temperature estimates from recent subduction models (e.g. Syracuse *et al.*, 2010), our study confirms the likelihood that melt ± fluid, particularly from an altered (high-K₂O) oceanic basalt protolith can transport important trace elements to the sources of arc magmas. Slab-top temperature imparts an important control on trace element concentrations in the melt and the ratios of key element pairs. In particular, oceanic crust can contribute melts with high ratios of Ba/Th and U/Th under conditions at which residual phengite is absent, but epidote is present. The results from our undoped starting materials

1
2
3
4
5
6
7
8
9
10
11
12
13
14
15
16
17
18
19
20
21
22
23
24
25
26
27
28
29
30
31
32
33
34
35
36
37
38
39
40
41
42
43
44
45
46
47
48
49
50
51
52
53
54
55
56
57
58
59
60

demonstrate the primacy of residual epidote as opposed to the LREE-rich allanite of previous, doped experimental studies.

ACKNOWLEDGEMENTS

This research was based in part on a Masters dissertation by LBC at the University of Bristol. We thank the workshop at Bristol for assistance with the piston cylinders; S. Kearns and B. Buse for help with the SEM and EMPA at Bristol; EIMF staff at the University of Edinburgh for help with SIMS analysis, and M. Guillong for help with the LA-ICP-MS at ETH. We would like to thank C. Till and an anonymous reviewer for helpful comments on an earlier version of this paper. The constructive reviews of J G. Prouteau, J. Adam, C. Spandler, and J Hermann (Editor) have further improved our manuscript, and were greatly appreciated.

FUNDING

This work was supported by grants from National Environmental Research Council [NE/G016615/1], the European Research Council [CRITMAG], and a Wolfson Research Merit Award to JB, and a Swiss National Science Foundation Ambizione grant [PZ00P2_142575] to SS.

REFERENCES

Adam, J., Green, T., Sie, S. & Ryan, C. (1997). Trace element partitioning between aqueous fluids, silicate melts and minerals. *European Journal of Mineralogy* **9**, 569–584.

- Alt, J., Anderson, T. & Bonnell, L. (1989). The geochemistry of sulfur in a 1.3 km section of hydrothermally altered oceanic crust, DSDP Hole 504B. *Geochimica et Cosmochimica Acta* **53**, 1011–1023.
- Avanzinelli, R., Prytulak, J., Skora, S., Heumann, A., Koetsier, G. & Elliott, T. (2012). Combined ^{238}U – ^{230}Th and ^{235}U – ^{231}Pa constraints on the transport of slab-derived material beneath the Mariana Islands. *Geochimica et Cosmochimica Acta* **92**, 308–328.
- Bach, W., Peucker-Ehrenbrink, B., Hart, S. R. & Blusztajn, J. S. (2003). Geochemistry of hydrothermally altered oceanic crust: DSDP/ODP Hole 504B - Implications for seawater-crust exchange budgets and Sr- and Pb-isotopic evolution of the mantle. *Geochemistry, Geophysics, Geosystems* **4**, 1–29.
- Barker, F. (1979). Trondhjemite: Definition, environment and hypotheses of origin. In: Barker, F. (ed.) *Trondhjemites, dacites, and related rocks*. Elsevier, 1–12.
- Bougault, H. & Cambon, P. (1979). Trace elements: Fractional crystallization and partial melting processes, heterogeneity of upper mantle material. *Initial Reports of the Deep Sea Drilling Project* **46**, 247–251.
- Cooper, L. B., Ruscitto, D. M., Plank, T., Wallace, P. J., Syracuse, E. M. & Manning, C. E. (2012). Global variations in $\text{H}_2\text{O}/\text{Ce}$: 1. Slab surface temperatures beneath volcanic arcs. *Geochemistry, Geophysics, Geosystems* **13**, 1–27.
- Cottrell, E. & Kelley, K. A. (2011). The oxidation state of Fe in MORB glasses and the oxygen fugacity of the upper mantle. *Earth and Planetary Science Letters* **305**, 270–282.
- Devey, C. W., Garbe-Schönberg, C.-D., Stoffers, P., Chauvel, C. & Mertz, D. F. (1994). Geochemical effects of dynamic melting beneath ridges: Reconciling major and trace element variations in Kolbeinsey (and global) mid-ocean ridge basalt. *Journal of Geophysical Research* **99**, 9077–9095.
- Droop, G. (1987). A general equation for estimating Fe^{3+} concentrations in ferromagnesian silicates and oxides from microprobe analyses, using stoichiometric criteria. *Mineralogical magazine* **51**, 431–435.
- Dungan, M., Rhodes, J., Long, P., Blanehard, D., Brannon, J. & Rodgers, K. (1979). Petrology and geochemistry of basalts from Site 396, Legs 45 and 46. *Initial Reports of the Deep Sea Drilling Project* **46**, 89–113.
- Elliott, T. (2003). Geochemical tracers of the slab. In: Eiler, J. (ed.) *Geophysical Monograph Series 138*. AGU, 23–45.

- 783 Elliott, T., Plank, T. & Zindler, A. (1997). Element transport from slab to volcanic front at
784 the Mariana arc. *Journal of Geophysical Research* **102**, 14991–15019.
- 785 Emmermann, R. & Puchelt, H. (1979). Abundances of rare earths and other trace elements
786 Leg 46 basalts (DSDP). *Initial Reports of the Deep Sea Drilling Project* **46**, 241–245.
- 787 Enami, M., Liou, J. & Mattinson, C. (2004). Epidote minerals in high P/T metamorphic
788 terranes: subduction zone and high- to ultrahigh-pressure metamorphism. *Reviews in*
789 *Mineralogy and Geochemistry*. AGU **56**, 347–398.
- 790 Frei, D., Liebscher, A., Franz, G. & Dulski, P. (2004). Trace Element Geochemistry of
791 Epidote Minerals. *Reviews in Mineralogy and Geochemistry* **56**, 553–605.
- 792 Frei, D., Liebscher, A., Wittenberg, A. & Shaw, C. S. J. (2003). Crystal chemical controls on
793 rare earth element partitioning between epidote-group minerals and melts: an
794 experimental and theoretical study. *Contributions to Mineralogy and Petrology* **146**,
795 192–204.
- 796 Gillis, K. & Robinson, P. (1988). Distribution of alteration zones in the upper oceanic crust.
797 *Geology* **16**, 262–266.
- 798 Green, T. H. & Adam, J. (2003). Experimentally-determined trace element characteristics of
799 aqueous fluid from partially dehydrated mafic oceanic crust at 3.0 GPa, 650–700°C.
800 *European Journal of Mineralogy* **15**, 815–830.
- 801 Guillong, M., Meier, D. L. Allan, M. M., Heinrich, C. A. & Yardley, B. W. D. (2008).
802 SILLS: A MATLAB-based program for the reduction of laser ablation ICP-MS data
803 of homogenous materials and inclusions. *Mineralogical Association of Canada Short*
804 *Course* **40**, 328–333.
- 805 Hermann, J. (2002a). Allanite: thorium and light rare earth element carrier in subducted
806 crust. *Chemical Geology* **192**, 289–306.
- 807 Hermann, J. (2002b). Experimental constraints on phase relations in subducted continental
808 crust. *Contributions to Mineralogy and Petrology* **143**, 219–235.
- 809 Hermann, J. & Green, D. H. (2001). Experimental constraints on high pressure melting in
810 subducted crust. *Earth and Planetary Science Letters* **188**, 149–168.
- 811 Hermann, J. & Rubatto, D. (2014). Subduction of Continental Crust to Mantle Depth:
812 Geochemistry of Ultrahigh-Pressure Rocks. In: Rudnick, R. L. (ed.) *Treatise on*
813 *Geochemistry (Second Edition)* **4: The Crust**. Elsevier, 309–340.
- 814 Hermann, J., Spandler, C., Hack, A. & Korsakov, A. (2006). Aqueous fluids and hydrous
815 melts in high-pressure and ultra-high pressure rocks: Implications for element
816 transfer in subduction zones. *Lithos* **92**, 399–417.

- 817 Hermann, J. & Spandler, C. J. (2008). Sediment Melts at Sub-arc Depths: an Experimental
818 Study. *Journal of Petrology* **49**, 717–740.
- 819 Hofmann, A. W. (1988). Chemical differentiation of the Earth: the relationship between
820 mantle, continental crust, and oceanic crust. *Earth and Planetary Science Letters* **90**,
821 297–314.
- 822 Humphris, S. & Thompson, G. (1978). Hydrothermal alteration of oceanic basalts by
823 seawater. *Geochimica et Cosmochimica Acta* **42**, 107–125.
- 824 Kagi, R., Muntener, O., Ulmer, P. & Ottolini, L. (2005). Piston-cylinder experiments on
825 H₂O undersaturated Fe-bearing systems: An experimental setup approaching fO₂
826 conditions of natural calc-alkaline magmas. *American Mineralogist* **90**, 708–717.
- 827 Kelley, K. A., Plank, T., Ludden, J. & Staudigel, H. (2003). Composition of altered oceanic
828 crust at ODP Sites 801 and 1149. *Geochemistry, Geophysics, Geosystems* **4**, 1–21.
- 829 Kessel, R., Schmidt, M. W., Ulmer, P. & Pettke, T. (2005a). Trace element signature of
830 subduction-zone fluids, melts and supercritical liquids at 120–180 km depth. *Nature*
831 **437**, 724–7.
- 832 Kessel, R., Ulmer, P., Pettke, T., Schmidt, M. W. & Thompson, A. B. (2005b). The water –
833 basalt system at 4 to 6 GPa : Phase relations and second critical endpoint in a K-free
834 eclogite at 700 to 1400°C. **237**, 873–892.
- 835 Klemme, S., Blundy, J. & Wood, B. (2002). Experimental constraints on major and trace
836 element partitioning during partial melting of eclogite. *Geochimica et Cosmochimica*
837 *Acta* **66**, 3109–3123.
- 838 Klimm, K., Blundy, J. D. & Green, T. H. (2008). Trace Element Partitioning and Accessory
839 Phase Saturation during H₂O-Saturated Melting of Basalt with Implications for
840 Subduction Zone Chemical Fluxes. *Journal of Petrology* **49**, 523–553.
- 841 Kogiso, T., Tatsumi, Y. & Nakano, S. (1997). Trace element transport during dehydration
842 processes in the subducted oceanic crust: 1. Experiments and implications for the
843 origin of ocean island basalts. *Earth and Planetary Science Letters* **148**, 193–205.
- 844 Konzett, J., Frost, D. J., Proyer, A. & Ulmer, P. (2007). The Ca-Eskola component in
845 eclogitic clinopyroxene as a function of pressure, temperature and bulk composition:
846 an experimental study to 15 GPa with possible implications for the formation of
847 oriented SiO₂-inclusions in omphacite. *Contributions to Mineralogy and Petrology*
848 **155**, 215–228.
- 849 Lambert, I. & Wyllie, P. (1972). Melting of gabbro (quartz eclogite) with excess water to 35
850 kilobars, with geological applications. *The Journal of Geology* **80**, 693–708.

- 851 Manning, C. (2004). The chemistry of subduction-zone fluids. *Earth and Planetary Science*
852 *Letters* **223**, 1–16.
- 853 Manning, C. E., Antignano, A. & Lin, H. A. (2010). Premelting polymerization of crustal
854 and mantle fluids, as indicated by the solubility of albite+paragonite+quartz in H₂O
855 at 1 GPa and 350–620°C. *Earth and Planetary Science Letters* **292**, 325–336.
- 856 Martin, L. A. J., Wood, B. J., Turner, S. & Rushmer, T. (2011). Experimental Measurements
857 of Trace Element Partitioning Between Lawsonite, Zoisite and Fluid and their
858 Implication for the Composition of Arc Magmas. *Journal of Petrology* **52**, 1049–
859 1075.
- 860 McDade, P., Wood, B. J., Van Westrenen, W., Brooker, R., Gudmundsson, G., Soulard, H.,
861 Najorka, J. & Blundy, J. (2002). Pressure corrections for a selection of piston-
862 cylinder cell assemblies. *Mineralogical Magazine* **66**, 1021–1028.
- 863 McDermott, F. & Hawkesworth, C. (1991). Th, Pb, and Sr isotope variations in young island
864 arc volcanics and oceanic sediments. *Earth and Planetary Science Letters* **104**, 1–15.
- 865 McMillan, P. F. & Holloway, J. R. (1987). Water solubility in aluminosilicate melts.
866 *Contributions to Mineralogy and Petrology* **97**, 320–332.
- 867 Melson, W. (1968). Volcanism and metamorphism in the Mid Atlantic Ridge, 22° N latitude.
868 *Journal of Geophysical Research* **73**, 5925–5941.
- 869 Molina, J. & Poli, S. (2000). Carbonate stability and fluid composition in subducted oceanic
870 crust: an experimental study on H₂O-CO₂-bearing basalts. *Earth and Planetary*
871 *Science Letters* **176**, 295–310.
- 872 Mottl, M. (1983). Metabasalts, axial hot springs, and the structure of hydrothermal systems
873 at mid-ocean ridges. *Geological Society of America Bulletin* **94**, 161–180.
- 874 Pearce, N. J. G., Perkins, W. T., Westgate, J. A., Gorton, M. P., Jackson, S. E., Neal, C. R. &
875 Chenery, S. P. (1997). A compilation of new and published major and trace element
876 data for NIST SRM 610 and NIST SRM 612 glass reference materials. *Geostandards*
877 *Newsletter* **21**, 115–144.
- 878 Pertermann, M. & Hirschmann, M. M. (2003). Anhydrous Partial Melting Experiments on
879 MORB-like Eclogite: Phase Relations, Phase Compositions and Mineral-Melt
880 Partitioning of Major Elements at 2–3 GPa. *Journal of Petrology* **44**, 2173–2201.
- 881 Plank, T., Cooper, L. B. & Manning, C. E. (2009). Emerging geothermometers for
882 estimating slab surface temperatures. *Nature Geoscience* **2**, 611–615.

- 883 Poli, S., Franzolin, E., Fumagalli, P. & Crottini, A. (2009). The transport of carbon and
884 hydrogen in subducted oceanic crust: An experimental study to 5 GPa. *Earth and*
885 *Planetary Science Letters* **278**, 350–360.
- 886 Prouteau, G. & Scaillet, B. (2012). Experimental Constraints on Sulphur Behaviour in
887 Subduction Zones: Implications for TTG and Adakite Production and the Global
888 Sulphur Cycle since the Archean. *Journal of Petrology* **54**, 183–213.
- 889 Prouteau, G., Scaillet, B., Pichavant, M. & Maury, R. (1999). Fluid-present melting of
890 oceanic crust in subduction zones. *Geology* **27**, 1111–1114.
- 891 Prouteau, G., Scaillet, B., Pichavant, M. & Maury, R. (2001). Evidence for mantle
892 metasomatism by hydrous silicic melts derived from subducted oceanic crust. *Nature*
893 **410**, 197–200.
- 894 Rapp, R. P. & Watson, E. B. (1995). Dehydration Melting of Metabasalt at 8–32 kbar:
895 Implications for Continental Growth and Crust-Mantle Recycling. *Journal of*
896 *Petrology* **36**, 891–931.
- 897 Ryabchikov, I. D., Miller, C. & Mirwald, P. W. (1996). Composition of hydrous melts in
898 equilibrium with quartz eclogites. *Mineralogy and Petrology* **58**, 101–110.
- 899 Sato, H., Aoki, K.-I., Okamoto, K. & Fujita, B.-Y. (1979). Petrology and chemistry of
900 basaltic rocks from hole 396B, IPOD/DSDP leg 46. *Initial Reports of the Deep Sea*
901 *Drilling Project* **46**, 115–141.
- 902 Schmidt, M. (1996). Experimental constraints on recycling of potassium from subducted
903 oceanic crust. *Science* **272**, 1927–1930.
- 904 Schmidt, M. W. & Poli, S. (1998). Experimentally based water budgets for dehydrating slabs
905 and consequences for arc magma generation. *Earth and Planetary Science Letters*
906 **163**, 361–379.
- 907 Schmidt, M. W. & Poli, S. (2014). Devolatilization During Subduction. In: Rudnick, R. L.
908 (ed.) *Treatise on Geochemistry (Second Edition)* **4**, 669–701.
- 909 Schmidt, M. W., Vielzeuf, D. & Auzanneau, E. (2004). Melting and dissolution of
910 subducting crust at high pressures: the key role of white mica. *Earth and Planetary*
911 *Science Letters* **228**, 65–84.
- 912 Seyfried, W., Berndt, M. & Seewald, J. (1988). Hydrothermal alteration processes at mid-
913 ocean ridges: constraints from diabase alteration experiments, hot spring fluids and
914 composition of the oceanic. *The Canadian Mineralogist* **26**, 787–804.

- 915 Skora, S. & Blundy, J. (2010). High-pressure Hydrous Phase Relations of Radiolarian Clay
916 and Implications for the Involvement of Subducted Sediment in Arc Magmatism.
917 *Journal of Petrology* **51**, 2211–2243.
- 918 Skora, S. & Blundy, J. (2012). Monazite solubility in hydrous silicic melts at high pressure
919 conditions relevant to subduction zone metamorphism. *Earth and Planetary Science*
920 *Letters* **321–322**, 104–114.
- 921 Spandler, C., Hermann, J., Arculus, R. & Mavrogenes, J. (2003). Redistribution of trace
922 elements during prograde metamorphism from lawsonite blueschist to eclogite facies;
923 implications for deep subduction-zone processes. *Contributions to Mineralogy and*
924 *Petrology* **146**, 205–222.
- 925 Spandler, C. & Pirard, C. (2013). Element recycling from subducting slabs to arc crust: A
926 review. *Lithos* **170–171**, 208–223.
- 927 Staudigel, H., Hart, S. & Richardson, S. (1981a). Alteration of the oceanic crust: processes
928 and timing. *Earth and Planetary Science Letters* **52**, 311–327.
- 929 Staudigel, H., Muehlenbachs, K., Richardson, S. H. & Hart, S. R. (1981b). Agents of low
930 temperature ocean crust alteration. *Contributions to Mineralogy and Petrology* **77**,
931 150–157.
- 932 Staudigel, H. & Plank, T. (1996). Geochemical fluxes during seafloor alteration of the
933 basaltic upper oceanic crust: DSDP Sites 417 and 418. In: Bebout, E., Scholl, W. &
934 Al., E. (eds.) *Geophysical Monograph Series* 96. AGU, 19–38.
- 935 Stolper, E. & Newman, S. (1994). The role of water in the petrogenesis of Mariana trough
936 magmas. *Earth and Planetary Science Letters* **121**, 293–325.
- 937 Sun, S.-S. & McDonough, W. F. (1989). Chemical and isotopic systematics of oceanic
938 basalts: implications for mantle composition and processes. *Geological Society,*
939 *London, Special Publications* **42**, 313–345.
- 940 Syracuse, E. M. & Abers, G. A. (2006). Global compilation of variations in slab depth
941 beneath arc volcanoes and implications. *Geochemistry, Geophysics, Geosystems* **7**,
942 1–18.
- 943 Syracuse, E. M., van Keken, P. E. & Abers, G. A. (2010). The global range of subduction
944 zone thermal models. *Physics of the Earth and Planetary Interiors* **183**, 73–90.
- 945 Thompson, G. (1983). Basalt-Seawater Interaction. In: Rona, P. A., Boström, K., Laubier, L.
946 & Smith, K. L. (eds.) *Hydrothermal Processes at Seafloor Spreading Centers: NATO*
947 *Conference Series IV: Marine Sciences* 12P, 225–278.

- 948 Tribuzio, R., Messiga, B., Vannucci, R. & Bottazzi, P. (1996). Rare earth element
 949 redistribution during high-pressure–low-temperature metamorphism in ophiolitic Fe-
 950 gabbros (Liguria, northwestern Italy): Implications for light REE. *Geology* **24**, 711–
 951 714.
- 952 Truckenbrodt, J., Ziegenbein, D. & Johannes, W. (1997). Redox conditions in piston
 953 cylinder apparatus: The different behavior of boron nitride and unfired pyrophyllite
 954 assemblies. *American Mineralogist* **82**, 337–344.
- 955 Ulmer, P. & Trommsdorff, V. (1995). Serpentine stability to mantle depths and subduction-
 956 related magmatism. *Science* **268**, 858–61.
- 957 Van Keken, P. E., Hacker, B. R., Syracuse, E. M. & Abers, G. A. (2011). Subduction
 958 factory: 4. Depth-dependent flux of H₂O from subducting slabs worldwide. *Journal*
 959 *of Geophysical Research* **116**, 1–15.
- 960 Van Keken, P. E., Kiefer, B. & Peacock, S. M. (2002). High-resolution models of
 961 subduction zones: Implications for mineral dehydration reactions and the transport of
 962 water into the deep mantle. *Geochemistry, Geophysics, Geosystems* **3**, 1–20.
- 963 Yasuda, A., Fujii, T. & Kurita, K. (1994). Melting phase relations of an anhydrous mid-
 964 ocean ridge basalt from 3 to 20 GPa: Implications for the behavior of subducted
 965 oceanic crust in the mantle. *Journal of Geophysical Research* **99**, 9401–9414.

FIGURE CAPTIONS

Figure 1: Phase proportions in experiments on MORB and AOC (Table 2). Mineral abbreviations are: grt=garnet; cpx=clinopyroxene; qtz/coe=quartz/coesite; ky=kyanite; *=trace epidote, +=trace Fe-Ti oxide, ^=trace rutile.

Figure 2: Representative back-scattered electron (BSE) images of experimental run products at different temperatures in MORB and AOC. Mineral abbreviations as in Fig. 1, plus rt=rutile, vap=vapour and ep=epidote. Partial melts are always microvesicular due to exsolution of water upon quench. In some experiments, we find clear evidence for the presence of a vapour phase in addition to glass, as evidenced by a second, larger generation

1
2
3
4
5
6
7
8
9
10
11
12
13
14
15
16
17
18
19
20
21
22
23
24
25
26
27
28
29
30
31
32
33
34
35
36
37
38
39
40
41
42
43
44
45
46
47
48
49
50
51
52
53
54
55
56
57
58
59
60

of vesicles often containing “fish egg” textured spherules (quenched silicate fraction of a fluid phase rich in dissolved silicates, *c.f.* Adam *et al.*, 1997).

Figure 3: (a) Al/Na+K+2Ca ratios of quenched glasses showing a trend from peraluminous to metaluminous compositions at higher temperatures. (b) The granite classification scheme of Barker (1979) indicating that the experimental partial melts are trondhjemitic to tonalitic in composition.

Figure 4: Major element chemistry of quenched glasses (on an anhydrous basis) showing systematic changes with temperature. Where SiO₂ decreases, Al₂O₃ systematically increases with increasing temperature. The general tendency for CaO to increase with increasing temperature is consistent with the progressive consumption of clinopyroxene and epidote during melting. Titanium oxide contents increase systematically with increasing temperature in the presence of rutile because of increasing solubility.

Figure 5: Trace element compositions of experimental glasses normalised to PUM (primitive upper mantle; Sun & McDonough, 1989). Starting compositions are shown as thick solid grey lines. At low temperatures trace element patterns are spiky, becoming smoother and approaching their levels in the starting materials as temperature increases. Fluid-mobile elements (e.g. alkalis) are the most enriched at all conditions. Light REE are strongly depleted in partial melts, due to the presence of residual epidote up to ~900°C. Glasses also show enrichment of Zr (over Nd), Hf (over Sm) and Li (over Y), although these

characteristics are rarely reflected in arc magmas because of the subsequent control exerted by mantle wedge peridotite.

Figure 6: Trace element chemistry of quenched glasses showing systematic changes with temperature. Different element groups behave differently with increasing temperature, e.g. HREE, Y and Sc concentrations increase with increasing temperature, in contrast to most fluid-mobile elements. The different trace element patterns can be related to the presence or absence of residual phases as well as the additional vapour.

Figure 7: Schematic subcritical silicate-H₂O diagram versus temperature at constant pressure (3 GPa) (after Manning, 2004). Note that this sketch does not attempt to illustrate the chemography of our bulk-rocks. Instead, the figure approximates melt-fluid equilibrium in a simplified case in which the bulk composition corresponds to the minimum melt (+ H₂O) of AOC and MORB. Different residual solid phases that are present in our experimental run products are ignored here. It is illustrated in the diagram that our experiments only constrain the temperature at which two fluids condense to a single fluid (solvus: dashed lines). However, the position along the abscissa is not constrained because we did not vary the experimental water content. It is therefore possible that two fluids would have been present at higher temperatures, had more water been added.

Figure 8: Variation of log Σ LREE (La-Sm) in glasses *versus* temperature. Solid curves are modelled Σ LREE using the allanite solubility equation (9) given in Klimm *et al.* (2008), for pure allanite ($X_{\text{all}}=1$), and for $X_{\text{all}}=0.3$ (approximating the composition found by Klimm *et*

1
2
3
4
5
6
7
8
9
10
11
12
13
14
15
16
17
18
19
20
21
22
23
24
25
26
27
28
29
30
31
32
33
34
35
36
37
38
39
40
41
42
43
44
45
46
47
48
49
50
51
52
53
54
55
56
57
58
59
60

1022 *al.*, 2008). The Σ LREE of our undoped experiments is significantly lower when compared to
1023 allanite-saturated experiments, because these elements are hosted in epidote.
1024
1025 *Figure 9.* (La/Sm)_{PUM} versus Ba/Th for mafic arc lavas worldwide (compilation of Elliott,
1026 2003). Superimposed are the chemical compositions of the experimental glasses of this
1027 study, as well as the sub-solidus experiments of Green & Adam (2003). Barium/Th ratios are
1028 highest in our melts at 800-850°C from an AOC source, where epidote is present (retaining
1029 Th) but phengite (retaining Ba) is absent. Conversely, at low, sub-solidus temperatures,
1030 residual phengite will retain Ba and reduce Ba/Th in the fluids. Thus elevated Ba/Th is
1031 favoured by a narrow temperature interval between phengite-out and epidote-out.

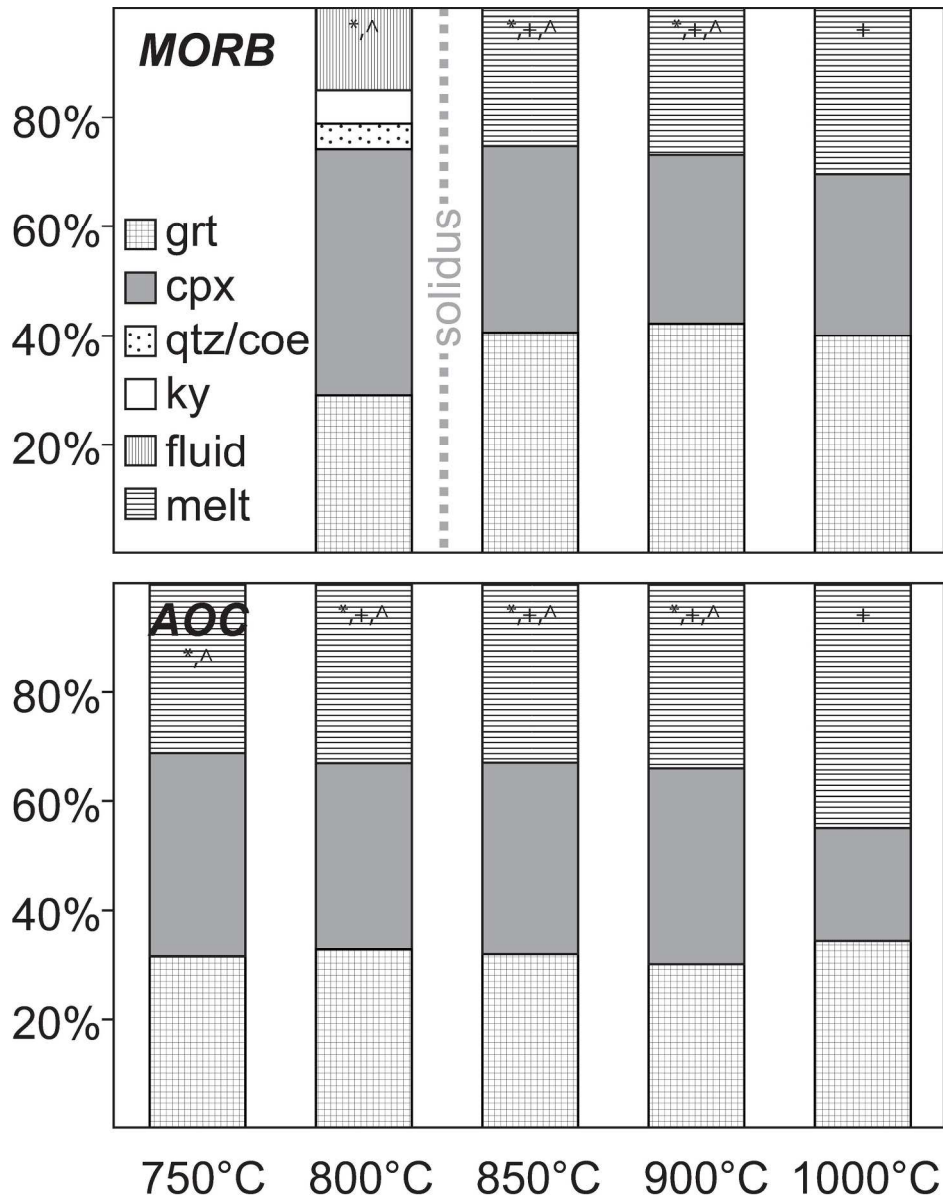


Figure 1
197x254mm (300 x 300 DPI)

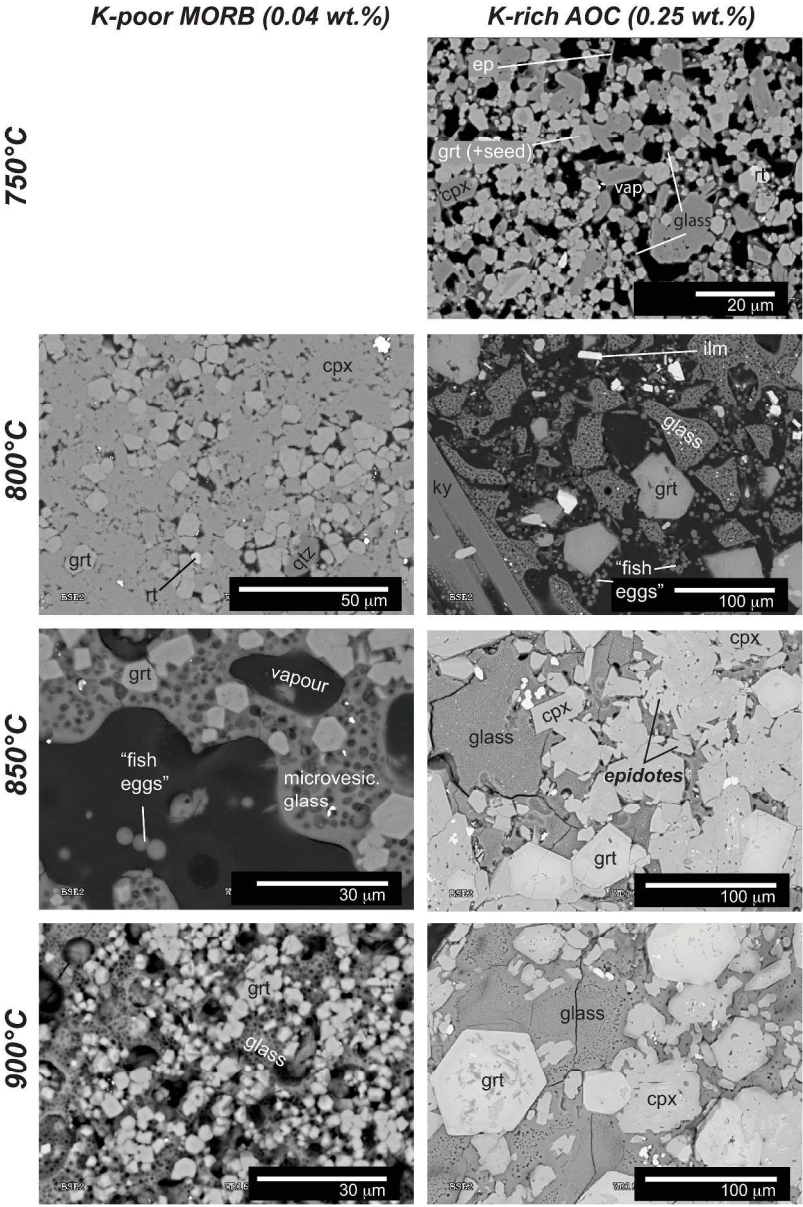


Figure 2
275x413mm (300 x 300 DPI)

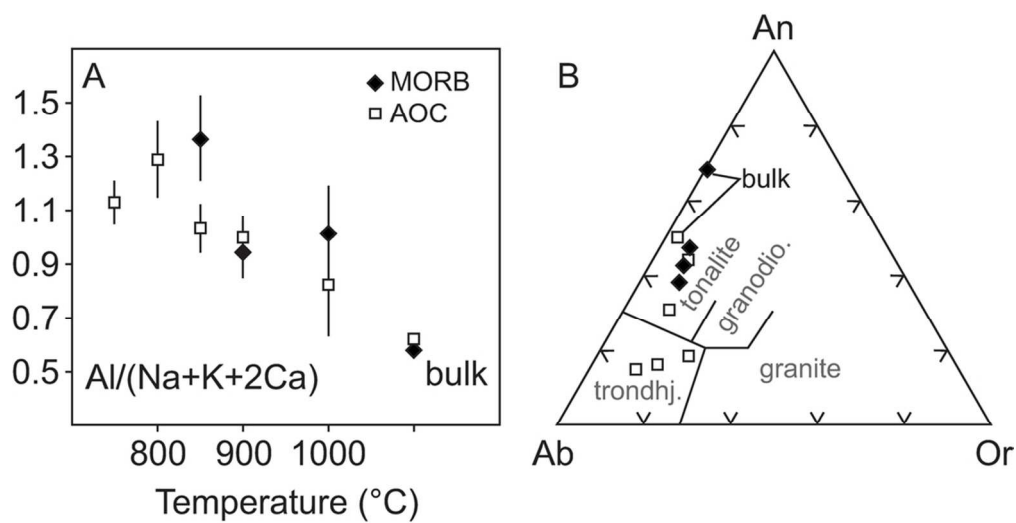


Figure 3
95x49mm (300 x 300 DPI)

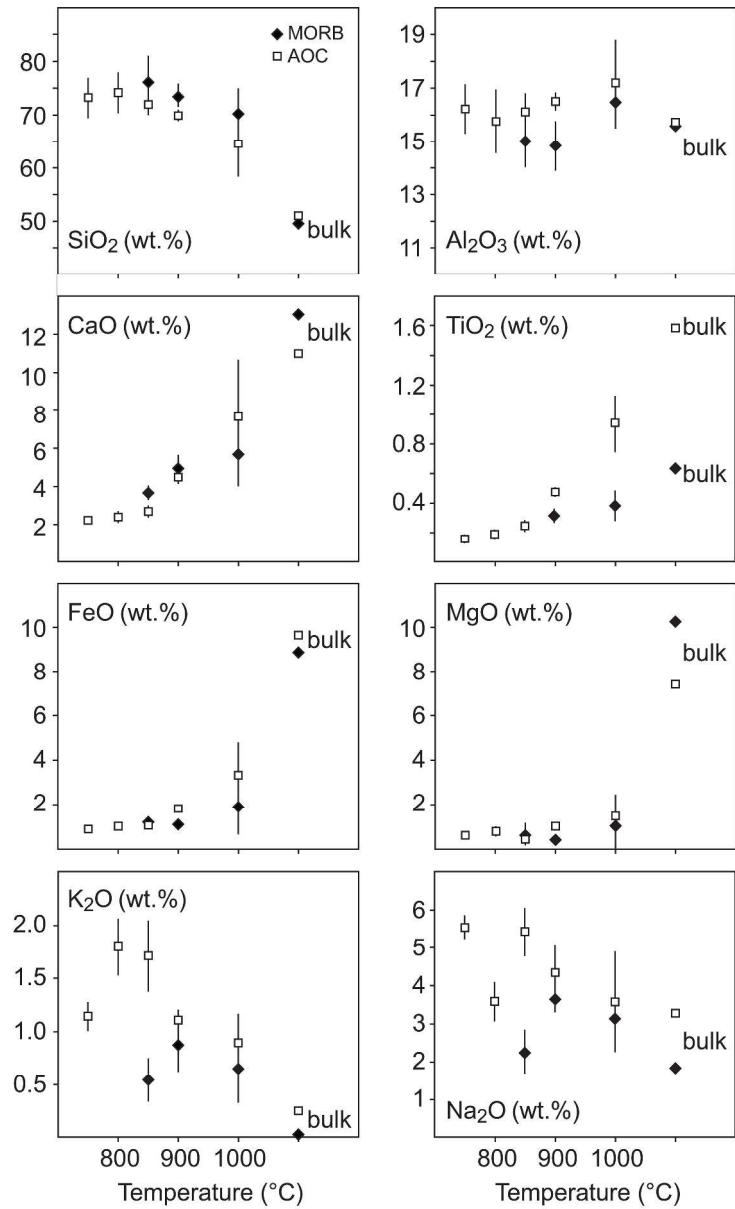


Figure 4
315x524mm (300 x 300 DPI)

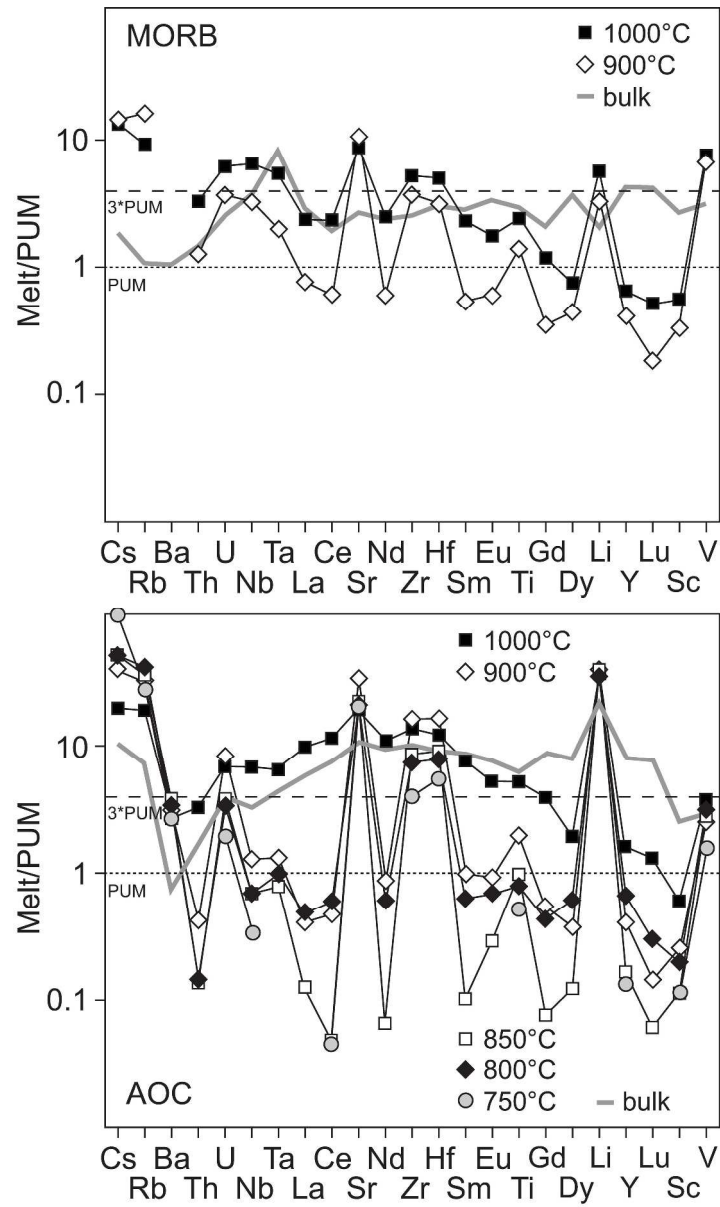


Figure 5
290x492mm (300 x 300 DPI)

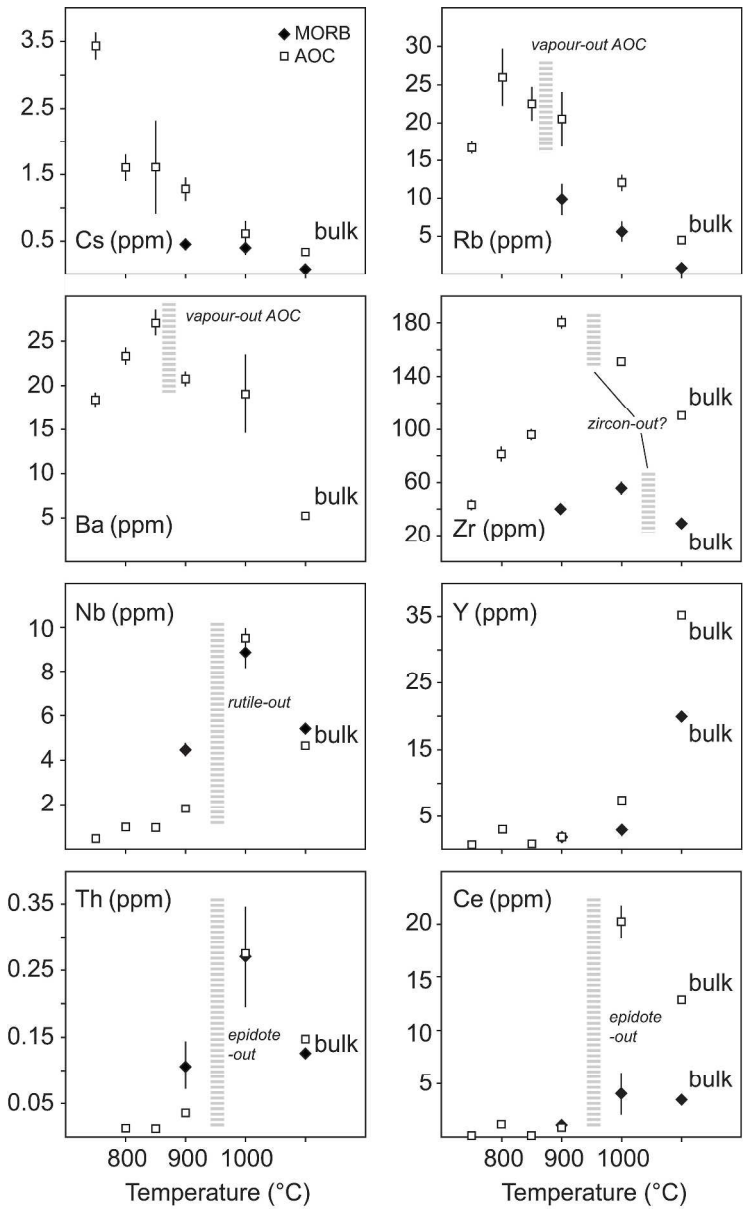


Figure 6
315x514mm (300 x 300 DPI)

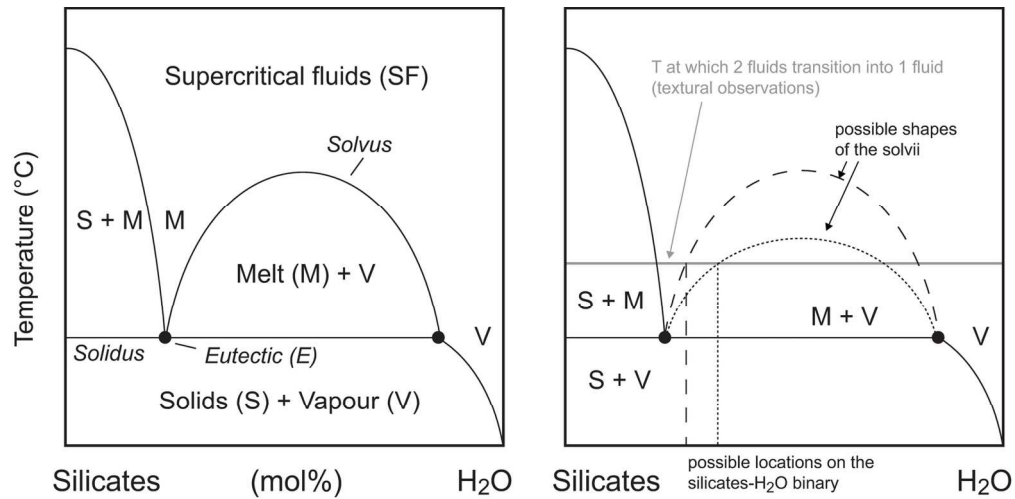


Fig.7
144x71mm (300 x 300 DPI)

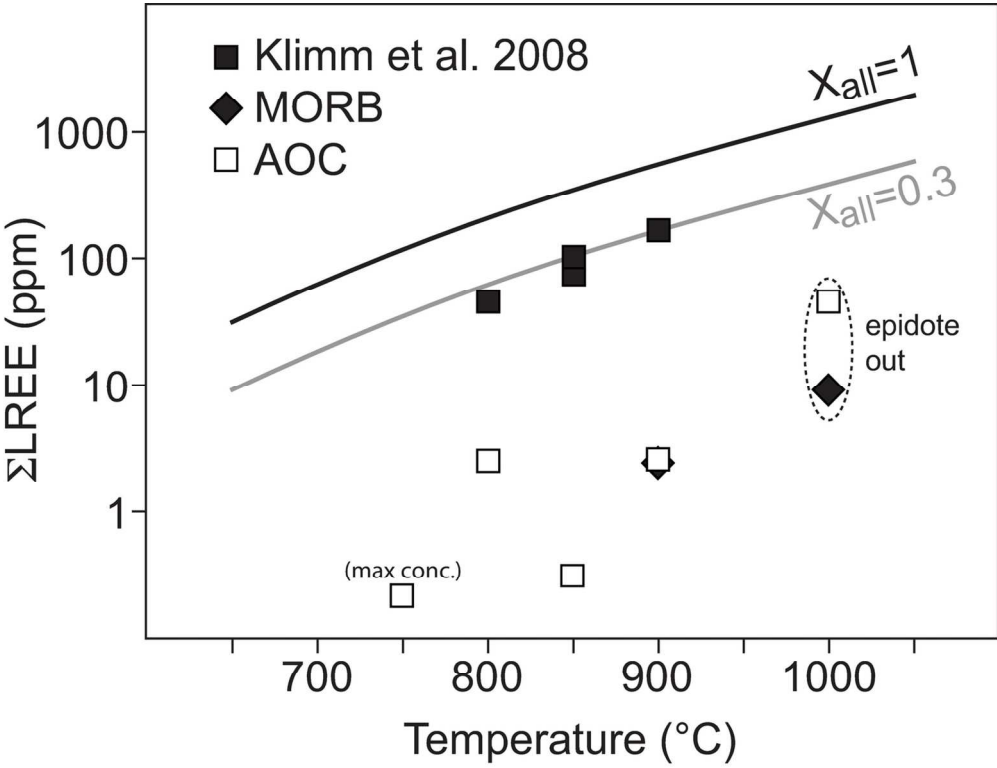


Fig.8
130x99mm (300 x 300 DPI)

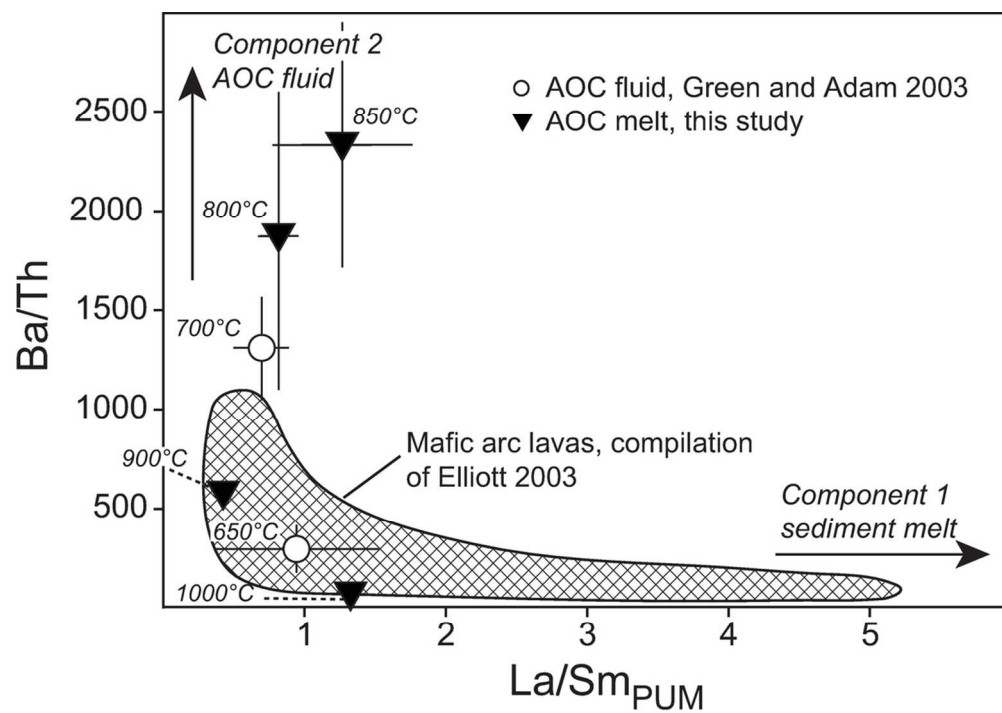


Figure 9
106x75mm (300 x 300 DPI)

1
2
3
4
5
6
7
8
9
10
11
12
13
14
15
16
17
18
19
20
21
22
23
24
25
26
27
28
29
30
31
32
33
34
35
36
37
38
39
40
41
42
43
44
45
46
47
48
49

Table 1. Starting compositions of basalts used in various experiments (TS=this study, Kessel 05a/b, Klimm08, G&A03), in comparison to natural compositions (Devey94, Hoff88, LEG-46, Kelley03)

Comp.	"Pristine" MORB						"Altered" MORB (AOC)						
Study	TS	TS	Dev94	Kess05a	Kess05b	TS	TS	LEG46	LEG46	Kelley03	Klimm08	G&A03	Hoff88
Type	MORB	Stdev	37DS-1	*Syn. MORB	Syn. MORB	AOC	Stdev	A3-Av	Stdev	Av. AOC Pacific	*Syn. AOC	*Oc. Tholeiite	Av. MORB
Majors (wt.%)													
n	20	20	1	-	-	40	40	12	12	117	-	-	26
SiO ₂	49.6	0.3	48.7	53.4	51.7	51.0	0.5	50.5	0.3	50.4	50.0	51.3	50.7
TiO ₂	0.63	0.02	0.64	1.45	1.52	1.58	0.04	1.66	0.02	1.74	1.17	1.89	1.62
Al ₂ O ₃	15.5	0.1	15.9	17.2	16.7	15.7	0.3	15.5	0.2	12.3	16.1	14.1	15.3
FeO _{tot}	8.9	0.2	10.1	8.50	9.98	9.6	0.2	10.0	0.2	12.5	11.7	12.2	10.5
MnO	0.18	0.04	0.18	-	-	0.13	0.03	0.20	0.01	0.23	0.10	0.19	-
MgO	10.3	0.1	10.1	5.93	7.03	7.4	0.1	7.7	0.3	6.36	7.16	6.55	7.62
CaO	13.0	0.1	12.7	10.2	9.92	11.0	0.1	10.9	0.1	13.3	10.2	10.5	11.4
Na ₂ O	1.83	0.08	1.71	3.24	3.17	3.3	0.1	3.0	0.1	2.35	3.31	2.80	2.69
K ₂ O	0.04	0.01	0.03	-	-	0.25	0.02	0.21	0.08	0.63	0.28	0.31	0.11
P ₂ O ₅	0.05	0.02	0.04	-	-	ND	ND	0.14	0.01	0.17	-	0.22	-
Sum	100	-	100	100	100	100	-	100	-	100	100	100	100
Mg#	0.67	0.01	0.64	0.55	0.56	0.58	0.01	0.58	0.01	0.48	0.52	0.49	0.56
Traces (ppm)													
n	5	5	1	-	-	5	5	4-12	4-12	117	-	-	26
Li	3.39	0.07	-	247	-	33.3	0.1	13	12	14.1	92	82.6	-
Sc	47	1	-	148	-	41.8	0.8	38	1	37.4	83	-	41.4
Ti	3880	60	-	8590	-	9034	248	9822	113	-	7010	11300	9740
V	265	6	-	-	-	233	4	282	5	338	48	355	-
Rb	0.7	0.2	0.58	84	-	4.4	0.5	1.9	1.1	13.7	-	102	1.26
Sr	56	1	55	113	-	214	3	137	5	109	36	210	113
Y	19.8	0.3	18.6	102	-	34	1	34.8	1.1	40.7	40	159	35.8

Zr	29.2	0.5	28	151	-	107	6	116	3	112	145	227	104
Nb	2.7	0.2	1.69	135	-	2.3	0.2	1.9	0.4	2.89	120	128	3.51
Cs	0.06	0.03	-	87	-	0.32	0.07	-	-	0.317	-	80.7	0.014
Ba	7.1	0.2	6.9	97	-	5.1	0.7	-	-	15.6	-	176	13.9
La	2.0	0.1	1.00	131	-	3.8	0.2	4.3	0.4	3.4	158	97.0	3.90
Ce	3.4	0.2	2.91	137	-	13	1	11.8	1.5	11.4	167	114	12.0
Nd	3.2	0.3	3.22	176	-	13	1	10.6	1.1	11.3	176	-	11.2
Sm	1.3	0.1	1.33	180	-	3.7	0.3	4.1	0.2	3.95	163	94.3	3.75
Eu	0.57	0.07	0.57	192	-	1.2	0.1	1.32	0.02	1.34	207	-	1.34
Gd	1.26	0.09	2.05	220	-	4.9	0.4	-	-	5.55	-	-	5.08
Dy	2.7	0.2	3.05	239	-	5.5	0.5	6.5	0.2	6.56	-	-	6.30
Lu	0.31	0.04	0.35	143	-	0.55	0.03	0.64	0.03	0.636	133	100	0.589
Hf	0.9	0.2	1.04	231	-	2.6	0.3	3.0	0.1	3.07	39	13.5	2.97
Ta	0.34	0.02	-	120	-	0.17	0.03	0.20	0.01	0.21	36	11.2	0.192
Th	0.13	0.01	-	229	-	0.14	0.03	0.15	0.01	0.173	268	106	0.187
U	0.06	0.03	-	241	-	0.08	0.02	-	-	0.390	257	102	0.071
ΣLREE	9.9	0.4	8.5	624	-	33	2	31	2	30	664	305	31

Major element analyses are recalculated on an anhydrous basis for comparison; trace element are given as published

- either not reported or not added to the experiment

Abbreviations used: Syn=synthetic; Av=average; Oc=oceanic; TS=this study; ND=not determined

* trace element doped compositions

LEG56-A3-Av: majors, Rb, Sr, Y, Zr, Nb: Dungan *et al.* (1979); Ti, V, Hf, Ta, Th: Bougault & Cambon (1979); Li, Sc, La, Ce, Nd, Sm, Eu, Dy, Lu: Emmermann & Puchelt (1979)

Hoff88=Hofmann (1988); Kess05a/b=Kessel *et al.* (2005a/b); Kelley03=Kelley *et al.* (2003); Klimm08=Klimm *et al.* (2008); G&A03=Green & Adam (2003); Dev94=Devey *et al.* (1994).

Table 2. Run conditions and phase proportions

<i>P</i> =3 GPa	time	Temp.	major phases in %									
Run	[days]	[°C]	grt	cpx	qtz/coe	(st [*])/ky	Fe-Ti	phen	liq	vapour	glass	trace phases
<i>MORB</i>												
LC2	7	800	29.1	44.9	4.7	6.2	-	-	15.0	X+FE	-	ep, rt
			34.3	52.9	5.5	7.3	-	-	-			
LC1	5	850	40.7	33.9	-	-	-	-	25.3	X+FE	X	ep, Fe-Ti, rt
			47.2	39.5	-	-	-	-	13.3			
LC3B	4	900	42.5	30.7	-	-	-	-	26.9	X	X	ep, Fe-Ti, rt
			49.2	35.5	-	-	-	-	15.3			
LC4	3	1000	40.7	29.3	-	-	-	-	30.2	-	X	Fe-Ti
			47.0	33.8	-	-	-	-	19.4			
<i>AOC</i>												
LCA0	8	750	-	59.6	5.9	15.9	1.7	1.8	15.0	X+FE	-	ep, rt, apa
			-	70.2	7.0	18.7	2.1	2.1	-			
LCA0 rep [#]	8	750	31.5	37.4	-	-	-	-	31.1	X	X	ep, rt, grt seeds
			36.3	43.1	-	-	-	-	20.6			
LCA2B	7	800	32.7	34.3	-	-	-	-	33.0	X+FE	X	ep, rt, Fe-Ti, ky
			37.6	39.5	-	-	-	-	22.9			
LCA1	5	850	31.8	35.4	-	-	-	-	32.7	(X)	X	ep, rt, Fe-Ti, ky
			36.6	40.8	-	-	-	-	22.7			
LCA3	4	900	30.3	35.7	-	-	-	-	34.0	-	X	ep, rt, Fe-Ti, ky
			34.8	40.9	-	-	-	-	24.3			
LCA4	3	1000	34.3	20.7	-	-	-	-	45.1	-	X	Fe-Ti
			38.8	23.4	-	-	-	-	37.8			

[#]LCA0 rep is a repeat experiment of LCA0, run with grt seeds at ETH Zürich, see Methods for more information
Abbreviations used: grt=garnet; cpx=clinopyroxene; qtz/coe=quartz/coesite; ky=kyanite; Fe-Ti=Fe-Ti oxide; phen=phengite; liq=bulk liquid; ep=epidote; rt=rutile; apa=apatite; FE="fish eggs"; (st^{*}) refers to the presence of staurolite as Al-rich phase in AOC sub-solidus experiment .
Mass balances were initially performed using anhydrous compositions (values in italic), and H₂O was later reintegrated (see text)

Table 3. Major and minor element compositions of experimental glasses

Exp. Type T (°C)	LC1 measured 850	LC1 SD 850	LC1 anhydr. 850	LC3B measured 900	LC3B SD 900	LC3B anhydr. 900	LC4 measured 1000	LC4 SD 1000	LC4 anhydr. 1000	LCA0 rep measured 750	LCA0 rep SD 750	LCA0 rep anhydr. 750
(wt %)	<i>MORB</i>	<i>MORB</i>	<i>MORB</i>	<i>MORB</i>	<i>MORB</i>	<i>MORB</i>	<i>MORB</i>	<i>MORB</i>	<i>MORB</i>	<i>AOC</i>	<i>AOC</i>	<i>AOC</i>
n	24	24	24	36	36	36	52	52	52	8	8	8
SiO ₂	60	4	76	57	2	74	54	3	71	58	3	73
TiO ₂	0.19	0.03	0.24	0.25	0.04	0.32	0.29	0.08	0.38	0.12	0.02	0.15
Al ₂ O ₃	11.9	0.8	15.0	11.5	0.7	14.8	12.6	0.8	16.4	12.8	0.7	16.2
FeO _{tot}	0.9	0.2	1.2	0.9	0.1	1.1	1.5	0.9	1.9	0.7	0.1	0.8
MgO	0.5	0.4	0.7	0.3	0.1	0.4	1	1	1	0.5	0.1	0.6
CaO	2.9	0.3	3.7	3.8	0.6	4.9	4	1	6	1.7	0.2	2.2
Na ₂ O	1.8	0.5	2.3	2.8	0.3	3.6	2.4	0.7	3.1	4.4	0.2	5.5
K ₂ O	0.4	0.2	0.5	0.7	0.2	0.9	0.5	0.3	0.7	0.9	0.1	1.1
P ₂ O ₅	0.2	0.1	0.2	0.2	0.1	0.3	0.1	0.1	0.1	0.11	0.04	0.14
Sum	79	5	100	78	2	100	77	3	100	79	4	100
Al/(K+Na+2Ca)	1.4	0.2	1.4	0.9	0.1	0.9	1.0	0.2	1.0	1.1	0.1	1.1
(Na+K)/Al	0.29	0.07	0.29	0.47	0.05	0.47	0.36	0.09	0.36	0.64	0.06	0.64
Mg#	0.5	0.4	0.5	0.4	0.2	0.4	0.5	0.8	0.5	0.6	0.2	0.6

Exp. Type T (°C)	LCA2B measured 800	LCA2B SD 800	LCA2B anhydr. 800	LCA1 measured 850	LCA1 SD 850	LCA1 anhydr. 850	LCA3 measured 900	LCA3 SD 900	LCA3 anhydr. 900	LCA4 measured 1000	LCA4 SD 1000	LCA4 anhydr. 1000
(wt %)	<i>AOC</i>	<i>AOC</i>	<i>AOC</i>	<i>AOC</i>	<i>AOC</i>	<i>AOC</i>	<i>AOC</i>	<i>AOC</i>	<i>AOC</i>	<i>AOC</i>	<i>AOC</i>	<i>AOC</i>
n	46	46	46	34	34	34	36	36	36	44	44	44
SiO ₂	59	3	74	61	2	72	61	1	70	54	5	65
TiO ₂	0.15	0.02	0.19	0.21	0.03	0.25	0.41	0.03	0.47	0.8	0.2	0.9
Al ₂ O ₃	12.5	0.9	15.7	13.6	0.6	16.1	14.3	0.3	16.5	14	1	17
FeO tot	0.8	0.1	1.0	0.9	0.2	1.1	1.6	0.1	1.8	3	1	3
MgO	0.6	0.2	0.8	0.3	0.2	0.4	0.9	0.1	1.0	1.3	0.8	1.5
CaO	1.9	0.2	2.4	2.3	0.3	2.7	3.9	0.3	4.5	6	3	8
Na ₂ O	2.8	0.4	3.6	4.6	0.5	5.4	3.8	0.6	4.3	3	1	4
K ₂ O	1.4	0.2	1.8	1.4	0.3	1.7	0.96	0.08	1.11	0.7	0.2	0.9
P ₂ O ₅	0.31	0.08	0.39	0.32	0.07	0.38	0.36	0.06	0.42	0.2	0.1	0.3
Sum	80	4	100	84	2	100	86.7	0.9	100.0	84	4	100
Al/(K+Na+2Ca)	1.3	0.1	1.3	1.0	0.1	1.0	1.0	0.1	1.0	0.8	0.2	0.8
(Na+K)/Al	0.50	0.07	0.50	0.67	0.08	0.67	0.51	0.07	0.51	0.4	0.1	0.4
Mg#	0.6	0.2	0.6	0.4	0.2	0.4	0.5	0.1	0.5	0.4	0.3	0.4

SD=refers to 1 sigma of n (number) analyses; anhydr.=anhydrous

Table 4. Major and minor element composition of "fish eggs".

Exp.	LC1	LC1	LC1	LCA2B	LCA2B	LCA2B
Type	measured	SD	anhydr.	measured	SD	anhydr.
T (°C)	850	850	850	800	800	800
(wt.%)	<i>MORB</i>	<i>MORB</i>	<i>MORB</i>	<i>AOC</i>	<i>AOC</i>	<i>AOC</i>
n	7	7	7	13	13	13
SiO₂	65	5	81	65	2	78
TiO₂	0.15	0.07	0.19	0.11	0.04	0.13
Al₂O₃	11	1	13	13	1	15
FeO tot	0.7	0.3	0.8	0.4	0.1	0.5
MgO	0.4	0.2	0.5	0.4	0.3	0.4
CaO	2.5	0.4	3.1	1.8	0.4	2.2
Na₂O	0.5	0.3	0.6	1.6	0.5	1.9
K₂O	0.31	0.03	0.39	1.2	0.3	1.4
P₂O₅	0.05	0.03	0.06	0.15	0.05	0.18
Sum	80	6	100	83	2	100

SD=refers to 1 sigma of n (number) analyses; anhydr.=anhydrous

Table 5. Trace element compositions of hydrous glasses

Exp.	LC3B	LC3B	LC4	LC4	LCA0*	LCA0*	LCA2B	LCA2B	LCA1	LCA1	LCA3	LCA3	LCA4	LCA4
Type	meas	stdev	meas	stdev	rep	rep	meas	stdev	meas	stdev	meas	stdev	meas	stdev
T (°C)	900	900	1000	1000	750	750	800	800	850	850	900	900	1000	1000
(ppm)	MORB	MORB	MORB	MORB	AOC	AOC	AOC	AOC	AOC	AOC	AOC	AOC	AOC	AOC
n	7	7	5	5	11	11	5	5	5	5	5	5	6	6
Li	5.1	0.8	9	2	-	-	38	7	63	9	65	3	58	6
Sc	5.6	0.4	10	2	1.9	0.3	3.4	0.3	1.9	0.2	4.4	0.6	10.3	0.6
Ti	1770	50	3040	420	655	31	1020	150	1270	140	2580	60	7000	340
V	530	40	600	150	131	9	260	20	230	20	209	5	310	30
Rb	10	2	6	1	16.7	0.9	26	4	23	2	20	4	12	1
Sr	220	10	180	60	415	12	440	20	470	10	720	30	400	20
Y	1.9	0.2	2.9	0.9	0.60	0.05	3.0	0.4	0.75	0.06	1.9	0.1	7.4	0.4
Zr	40.3	0.9	56	5	43	2	81	6	96	3	181	5	151	4
Nb	2.2	0.1	4.4	0.3	0.24	0.03	0.50	0.09	0.49	0.06	0.92	0.06	4.8	0.2
Cs	0.4	0.1	0.4	0.1	3.4	0.2	1.6	0.2	1.6	0.7	1.3	0.2	0.6	0.2
Ba	-	-	-	-	18.4	0.8	23.3	0.9	27	1	20.7	0.8	19	4
La	0.52	0.06	1.6	0.8	<0.04	-	0.34	0.08	0.09	0.02	0.28	0.07	6.7	0.6
Ce	1.1	0.3	4	2	0.08	0.02	1.1	0.1	0.09	0.01	0.9	0.1	20	2
Nd	0.8	0.2	3	2	<0.02	-	0.8	0.1	0.09	0.06	1.2	0.2	15	2
Sm	0.24	0.08	1.0	0.6	<0.02	-	0.28	0.03	0.05	0.02	0.4	0.1	3.4	0.3
Eu	0.10	0.04	0.3	0.2	<0.06	-	0.12	0.06	0.05	0.04	0.16	0.03	0.89	0.05
Gd	0.21	0.03	0.7	0.3	<0.03	-	0.26	0.04	0.05	0.02	0.32	0.07	2.3	0.2
Dy	0.32	0.06	0.5	0.3	0.08	0.02	0.5	0.1	0.09	0.03	0.28	0.06	1.4	0.2
Lu	0.014	0.006	0.04	0.01	<0.02	-	0.022	0.004	<DL	<DL	0.011	0.004	0.10	0.02
Hf	0.9	0.2	1.5	0.2	1.6	0.2	2.4	0.2	2.8	0.3	5.1	0.4	3.7	0.3
Ta	0.08	0.01	0.22	0.05	<0.03	-	0.04	0.01	0.03	0.02	0.05	0.01	0.27	0.05
Th	0.11	0.04	0.27	0.08	<0.02	-	0.012	0.005	0.012	0.003	0.036	0.003	0.28	0.04
U	0.07	0.02	0.12	0.06	0.04	0.01	0.07	0.02	0.08	0.04	0.17	0.04	0.14	0.04

ΣLREE	2.6	0.4	10	3	<0.2	-	2.5	0.2	0.3	0.1	2.7	0.2	45	2
Ba/Th	460	180	130	40	>920	-	1870	770	2330	610	580	50	70	20
La/Sm_{PUM}	1.5	0.3	1.1	0.5	-	-	0.8	0.1	1.3	0.5	0.4	0.1	1.3	0.1
U/Th_n	2	1	1.0	0.8	>3.5	-	10	6	12	9	9	4	0.9	0.4

*Experiment analyzed by LA-ICP-MS, all other exp are analyzed by SIMS; Ba concentrations for AOC are LA-ICP-MS data, see methods for more details

ΣLREE=SUM (La-Sm); La/Sm_{PUM} are PUM normalized; U/Th_n are source normalized

Analyses below detection limits (DL) are reported as <DL.